Supporting Information for:

Self-Supported Ultra-Active NiO-Based Electrocatalysts for Oxygen Evolution Reaction by Solution Combustion.

Alberto Bucci,[a,*] Miguel García-Tecedor,[b,e] Sacha Corby,[c] Reshma Rao,[c] Vlad Martin-Diaconescu,[d] Freddy E. Oropeza,[e] Víctor A. de la Peña O'Shea,[e] James R. Durrant,[c,f,] Sixto Giménez,[b,*] Julio Lloret-Fillol[a,g,*]

[a] Institute of Chemical Research of Catalonia (ICIQ), The Barcelona Institute of Science and Technology, Avinguda Països Catalans 16, 43007 Tarragona, Spain.

[b] Insitute of Advanced Materials (INAM), University Jaume I, 12071 Castello de la Plana, Spain

[c] Department of Chemistry and Centre for Plastic Electronics, Imperial College London, London W12 0BZ, U.K.

[d] CELLS−ALBA Synchrotron E-08290 Cerdanyola del Vallès, Barcelona, Spain

[e] Madrid Photoactivated Processes Unit, IMDEA Energy Institute, Av. Rámon de la Sagra, 3 Parque Tecnologico de Mostoles, 28935, Mostoles, Madrid, Spain

[f] SPECIFIC, College of Engineering, Swansea University, Bay Campus, Fabian Way, Swansea SA1 8EN, U.K.

[g] Catalan Institution for Research and Advanced Studies (ICREA), Passeig Lluïs Companys, 23, 08010, Barcelona (Spain).

* corresponding authors: e-mail: abucci@iciq.es (AB); sjulia@fca.uji.es (SG); jlloret@iciq.es (JL-F)

Table of Contents

1. General Procedures

1.1 Synthetic Protocols

Materials and reagents. Commercial reagents and solvents were purchased from Sigma Aldrich and Alfa Aesar and used as received without further purification. NF was purchased by Goodfellow and FTO by Sigma Aldrich. KOH electronic grade 99.98% was provided by Alfa Aesar and purified before use (see below).

Synthesis of undoped NiO. Undoped NiO was synthetized in one-pot SC synthesis by mixing in 10 mL of MilliQ water 350 mg of $Ni(NO_3)_2(H_2O)_6$ with ethylene glycol (67 μL) in the ratio 1:0.95 for a final metal concentration of 0.12 M. The combustion mixture was stirred for 1 h before transferring inside a muffle furnace. Two gradients temperature were applied: an initial fast ramp of 10 °C/min up to 100 ºC, followed by a slower one of 2 °C/min, until a final T = 350 ºC was reached. Only 5 minutes of soaking connects the two ramps, whereas, at the end of the second, the sample was allowed to stay for 1 hour.

Synthesis M-NiO. This synthesis was repeated identically to that of NiO, but this time to the combustion mixture, 10% of $M^{n+}Cl_n$ was added. In particular, a solution 0.24 M of the dopant salt was prepared by dissolving the corresponding precursor in ultra-pure water and 500 μL of this solution were injected in the vial containing Ni^{2+}/EG precursors (0.12 M, 10 mL).

Synthesis NiO@NF and M-NiO@NF. This synthesis was repeated adjusting concentrations respect to those already discussed. Two equimolar solutions (0.5 M) of $Ni(NO_3)_2$ and $M^{n+}Cl_n$ were separately prepared. EG was added to the Ni solution in order to obtain a 1:0.95 metal fuel ratio. Finally, the Ni and EG solution was mixed with the dopant one in a 9:1 ratio in order to keep the final metal concentration at 0.5 M. The new solution was allowed to stir one hour before a pre-cleaned piece of NF was dip-coated in combustion vial. For dip coating, NF was kept 180 seconds immersed into the combustion mixture and successively removed from the vial and transferred in a flat porcelain crucible. The latter was then placed into a pre-heated muffle furnace at 180 °C during 2 min to allow the combustion to occur. The as-prepared electrode was rinsed with abundant ultra-pure water and sonicated for 30 seconds in acetone, before dried under a nitrogen stream. The electrode was also covered by epoxy resin and Kapton tape to ensure good insulation of the electrical contact (see below).

Picture S1. Comparison of bare NF (left) and NF after growing $Fe_{0.1}$-NiO by combustion synthesis (right).

Synthesis of $Fe_{0.1}$-NiO@NF - TND. The synthesis was carried out identically to that of the analogous SC sample, but in the absence of the fuel.

1.2 Physico-Chemical Characterization

Powder X-ray diffraction (PXRD): PXRD patterns of NiO and M-NiO powder samples were recorded on a D8 Advance Series 2Theta/Theta powder diffraction system using CuKα1-radiation in transmission geometry. The system is equipped with a VÅNTEC-1 single-photon counting PSD, a Germanium monochromator, a ninety positions auto changer sample stage, fixed divergence slits and a radial soller. The angular 2θ diffraction range was between 5 and 70°. The data were collected with an angular step of 0.02° at 12 s per step and sample rotation.

Fourier-Transformed Infrared (FTIR) Spectroscopy: FTIR measurements were carried out on a Bruker Optics FT-IR Alpha spectrometer equipped with a DTGS detector, KBr beamsplitter at 4 cm^{-1} resolution using a one bounce ATR accessory with diamond windows.

Scanning Electron Microscopy (SEM): The ESEM is from FEI company, model Quanta 600 in low vacuum mode (vacuum pressure 0.68 Torr). The EDX is from Oxford Instruments. The conditions for the ESEM are 20kV accelerating voltage and working distance close to 10 mm.

Transmission electron microscopy (**TEM):** TEM images were collected using a JEOL 1011 Transmission Electron Microscope operating at 80 kV. Samples were dispersed in ethanol and a drop of resultant suspensions was poured on carbon coated-copper grids.

XPS Data Collection: XP spectra were recorded using a SPECS NAP-XPS System incorporating the DeviSim NAP reaction cell. The spectrometer is equipped with a Al Kα monochromated source (hν = 1486.6 eV), composed of a SPECS XR50 MF X-ray gun

and a μ-FOCUS 600 monochromator, and PHOIBOS 150 NAP 1D-DLD analyser. X-ray gun power was set to 50 W (1.68 mA emission current and 13 kV) with a 300 μm^2 x-ray spot With this x-ray settings, the intensity of the Ag $3d_{5/2}$ photoemission peak for a Ag sample, recorded at 20 eV pass energy (PE), was 1×10^4 cps and the full width at half maximum (FWHM) was 0.60 eV. Binding energy calibration was made using Au $4f_{7/2}$ (84.01 eV), Ag $3d_{5/2}$ (368.20 eV) and Cu $2p_{3/2}$ (932.55 eV). The survey scans were acquired using 40 eV pass energy, 1 eV step size and 10 seconds (500 ms x 20 scans) dwell times. All high-resolution spectra were acquired using 20 eV pass energy, 0.1 eV step size and 75 seconds (1s x 75 scans) dwell times. The sample was analysed at an electron take-off angle normal to the surface with respect to the analyser.

Sample mounting: the electrode was pressed onto carbon based double side sticky tape. No significant signs of charging were observed.

XAS. Samples for metal K-edge X-ray absorbance were measured in fluorescence using a 36 element Ge detector as FTO-plated samples accordingly to the procedure described below. Data was acquired at the SOLEIL synchrotron SAMBA beamline. Measurements were taken at 25 K using a liquid helium cryostat and a Si(220) double crystal monochromator. Reference data collected in transmission on diluted pelleted powders, for $Co(OH)_2$, Fe_2O_3, Mn_2O_3, and MnO_2 was provided by the ALBA CLAESS beamline. The Athena software package was used for data calibration normalization and EXAFS data extraction.[1] Energies were calibrated to the first inflection point of metal foils taken as 6539 for Mn, 7111.2 for Fe, 7709.5 for Co and 8331.6 for Ni. For EXAFS analysis, Initial models were constructed with the Artemis software program running the IFEFFIT engine and the FEFF6 code.[2-3] Refinement of coordination number and S_0^2 square values, including multi k-weight fitting, aimed at minimizing correlations between disorder parameters and coordination numbers, were carried out with Larch, the Python implementation of Artemis.[4]

As such a grid search optimization was carried out with the coordination numbers modeled as $S_0^2 * \alpha_x *$(theoretical path degeneracy), where α is a fixed constant cycled between 0 and 1.2 in steps of 0.08 and x refers to the coordination shells with 1 being the metal-oxygen, 2 metal-metal and 3 higher coordination shells. The coordination numbers for the three regions were optimized simultaneously, exploring all resulting combinations. The (k^2,k^3)-weighted data was fit in r-space using a Hannings window (dk=1) over k- and

an r-ranges as specified in the text. Global S_0^2 and ΔE_0 values were employed with the initial E_0 value set to the inflection point of the rising edge. Single and multiple scattering paths were fit in terms of a Δr_{eff} and σ^2 as previously described. To assess the goodness of the fits both the R_{factor} (%R) and the reduced χ^2 (χ^2_v) were minimized, ensuring that the data was not over-fit.[5-6]

Pre-edge features in the XANES region were fit using a Gaussian-Lorentzian sum function with 50% Gaussian character.

1.3 Electrochemistry

Electrodes preparation. In order to evaluate the catalytic performances of the as-synthetized materials, in-depth electrochemical studies were carried out using two different electrode supports, i.e. nickel foam (NF size 20 x 10 x 0.9 mm^3) and FTO (25 x 10 mm^2). The deposition technique depends on the support: SC was used for NF and spray coating for FTO. In both cases, the geometric surface area was fixed to 1 cm^2.

For long-term CP experiments the electrode preparation foresaw also the insulation of the electrical contact, obtained by simple contacting Cu wire. Half of the electrode surface (10 x 10 mm^2) was sealed with epoxy resin and covered by Kapton tape. The remaining exposed surface (10 x 10 mm^2) was available for the catalysis.

For the spray coating, 5 mg of the catalyst were dispersed in 1 mL of a solution of 987 µL of EtOH/H_2O (3/1) and 12.7 µL of FAA Fumatech anionomer (ca. 10% w/w respect to the catalyst). Four coatings of 125 µL each (for a total of 500 µL) of such a dispersion were sprayed with an airbrush onto an FTO glass slide whose surface was entirely covered by a Kapton tape, except an exposed area of 10 x 10 mm^2. In order to ensure a fast deposition and homogeneous film, the FTO was placed on a hot plate at 75 °C during the entire process.

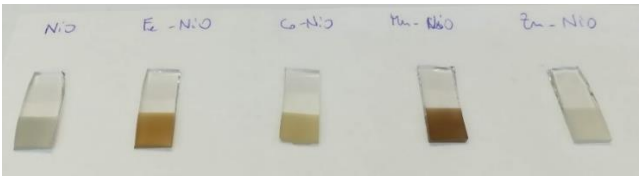

Picture S2. Picture representing as-deposited NiO and M-NiO films onto FTO by spray-coating.

Electrochemical Tests. For electrochemical tests, a standard sequence of experiments was used for each catalyst, involving an initial CV (10 mV/s) of 3-6 cycles, until the electrode was stabilized, then, linear sweep voltammograms (LSVs) were run with a scan rate of 5mV/s. All the voltammetry experiments were corrected accounting for ohmic loss iR_u, determined by electrochemical impedance spectroscopy (EIS). EIS experiments were conducted in the potential window 0 – 1 V vs Hg/HgO RE and a frequency range between 300 kHz and 0.1 Hz with an AC amplitude of 25 mV. Long-term chronopotentiometries (CP) were performed for 24 hours carefully degassing the solution by fluxing N_2 in order to remove oxygen (see Faradaic efficiency below)

TOF_{redox} values were calculated only when FTO was used, because of the impossibility to determine the final loading of the material in the NF after the combustion:

$$\mathrm{TOF_{redox}} = \frac{\mathrm{J_{geom}}}{4 * \mathrm{q}}$$

Where q is the integrated charge of the cathodic Ni redox wave.

The ECSA was determined by sweeping the potential in a 0.1 V window around the OCP at different scan rates (1 mVs^{-1}; 2.5 mVs^{-1}; 5 mVs^{-1}; 10 mVs^{-1}; 15 mVs^{-1} and 20 mVs^{-1}). The vertex potentials were held for 10 seconds before starting the reverse scan. The values of the anodic and cathodic currents were then plotted as a function of the scan rate and from the linear fit, the values of C_{DL} are obtained for different catalysts. The ECSA is then obtained by dividing the C_{DL} by the specific capacitance (40 $\mu F/cm^2$).

Impedance Spectroscopy. The EIS raw data were fitted using EC-Lab software. Nyquist plot appearance depends on the potential region adopted for the measurement. In the pre-catalytic region, the impedance response consists of the typical blocking electrode, as a consequence, the electrical circuit adopted for the fitting is constituted by only the ohmic resistance (R_Ω), in series with a constant phase element (CPE), which accounts for the deviation from the ideal behavior of a capacitor. On the other side, at the OER region, the Nyquist plot shows a depressed arc, characterized by its specific time constant due to the faradic process occurring under the anodic potential applied. The low-frequency intercept of such arc with the real part of the impedance is the resistance associated to OER, R_{LF}. Therefore, EIS data were fitted using a Randles circuit as kinetic model, in which, R_Ω is added in series with a parallel circuit constituted by the CPE and R_{LF}. When FTO was

used two semicircles appears in the OER region, one in the high-frequency window and another one in the low-frequency part.

Mott-Schottky analysis: Mott-Schottky analysis was carried out using the expression:

$$\frac{1}{C_{SC}^2} = \frac{2}{\varepsilon_0 \varepsilon_r e N_A A^2}\left(\phi_{SC} - \frac{kT}{e}\right), \text{ where } \phi_{SC} = V - V_{FB}$$

C_{SC} represents space charge capacitance, e is the elementary charge, ε_0 is the permittivity in vacuum, ε_r is the relative permittivity of NiO_x, (taken as 9.1)[7], N_A is the acceptor density, A is the area, k is the Boltzmann constant and T is the absolute temperature, taken as 298 K. From this analysis, the values of the flat-band potential (V_{FB}) and the acceptor density (N_A) were extracted.

Faradaic Efficiency. On-line analysis of the gas mixture during long-term CP experiment was performed by connecting the electrochemical cell to a micro-GC (Agilent 490 micro gas chromatograph, equipped with a thermal conductivity detector and a Molesieve 5Å column, calibrated with different $O_2/H_2/He$/ mixtures of known composition). O_2 was almost fully removed from the electrolyte using a constant N_2 flux of 30 mL/min (fixed with a mass-flow controller, Alicat®). During the CP experiment, the GC autosampler withdraws an aliquot of the headspace each 10 min, during at least 4 hours. The amount of O_2 and H_2 in moles was determined by the following equation:

$$\text{mol gas} = [(I - I_0)I_{Cal}]\frac{F\,t}{V_m}$$

where I is the measured signal, I_0 is the initial value of the signal (in the case of O_2 it is the residual amount of oxygen in solution), I_{cal} arises from the calibration, F is the flux (30 mL/min), t is the time, whereas V_m is the molar volume (22.414 L/mol).

2. Synthesis and characterization.

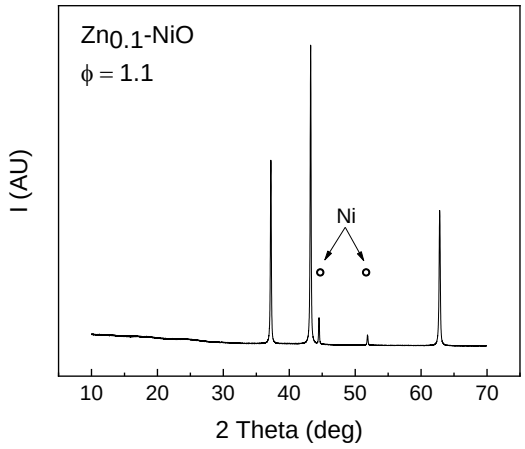

Figure S1. Zn-doping performed using ϕ = 1.1 during combustion synthesis, demonstrating that small excess of fuel produces Ni phase (open circles).

Table S1. Results of ICP-OES analysis of doped materials in atomic percentage.

	%Co	%Fe	%Mn	%Zn
NiO	0	0	0	0
$Co_{0.1}$-NiO	10			
$Fe_{0.1}$-NiO		8		
$Fe_{0.2}$-NiO		24		
$Fe_{0.3}$-NiO		31		
$Fe_{0.4}$-NiO		40		
$Mn_{0.1}$-NiO			9	
$Zn_{0.1}$-NiO				7

2.1 Microscopies

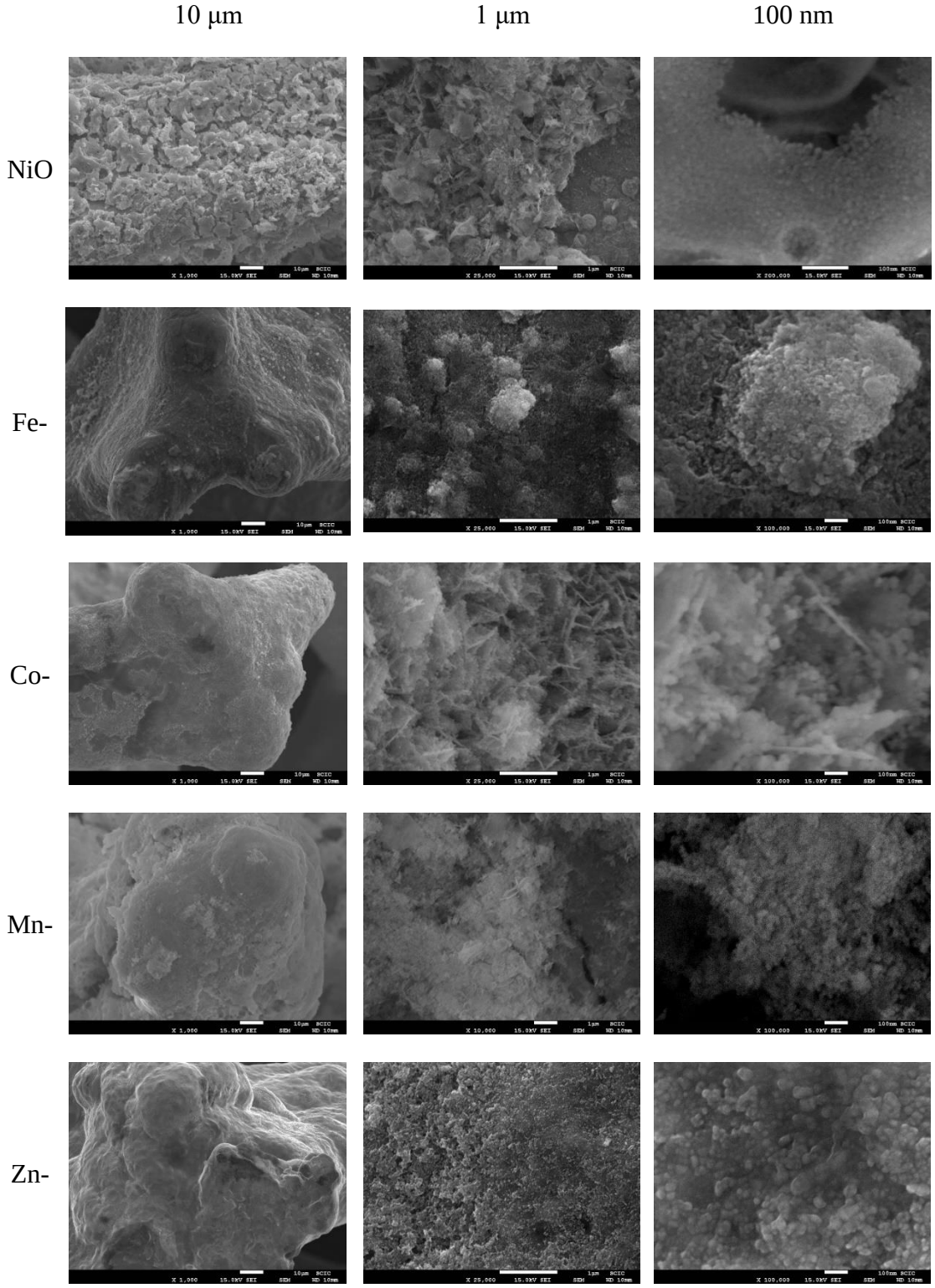

Figure S2. SEM images of (from first to last row) NiO/NF, $Fe_{0.1}$-NiO/NF, $Co_{0.1}$-NiO/NF, $Mn_{0.1}$-NiO/NF and $Zn_{0.1}$-NiO/NF, respectively, at different level of magnification.

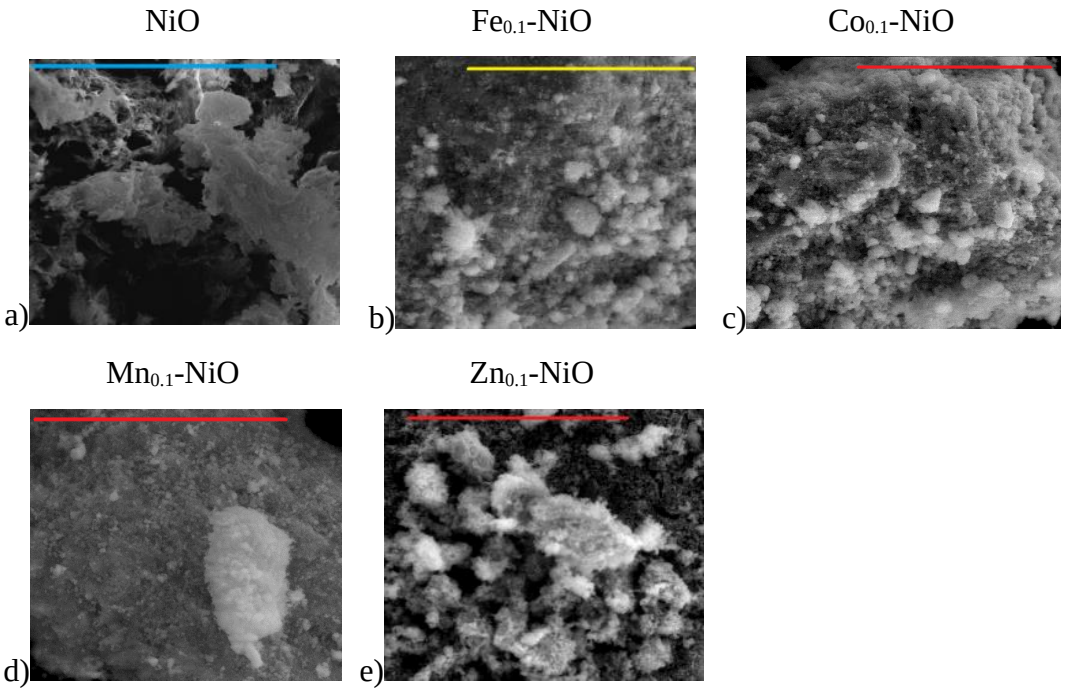

Figure S3. ESEM images of NiO (a), $Fe_{0.1}$-NiO (b), $Co_{0.1}$-NiO (c), $Mn_{0.1}$-NiO (d) and $Zn_{0.1}$-NiO (e), respectively at different level of magnification (blue scale bar = 10 μm, yellow bar = 50 μm and red bar = 40 μm).

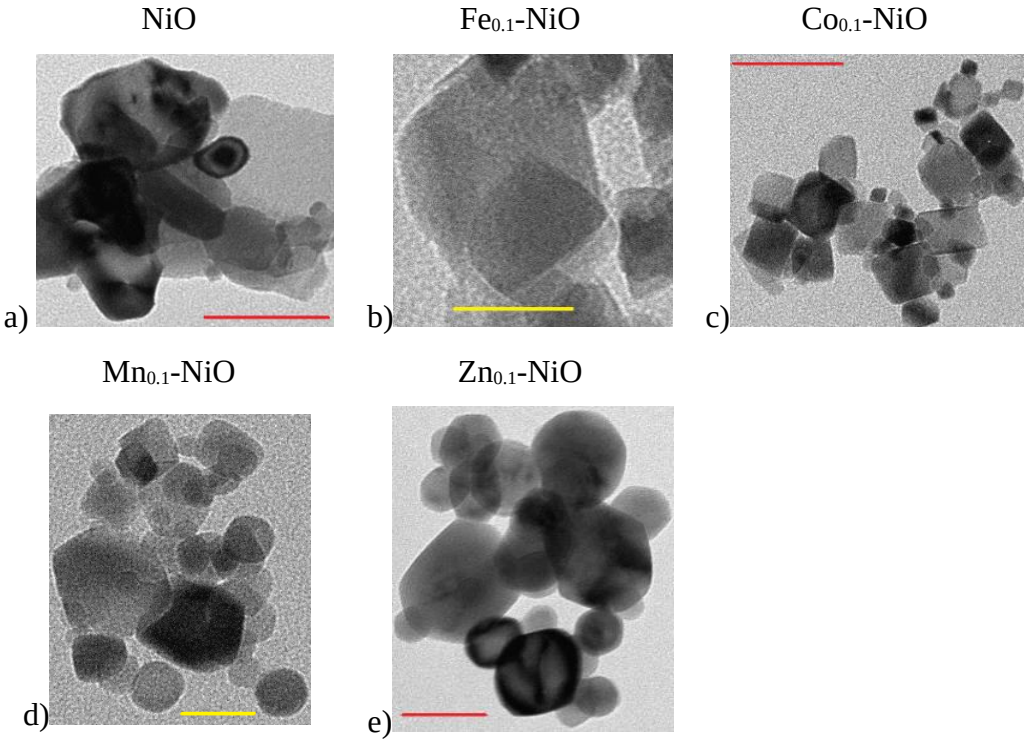

Figure S4. TEM pictures of NiO and M-NiO (red bars = 50 nm, yellow bars = 20 nm)

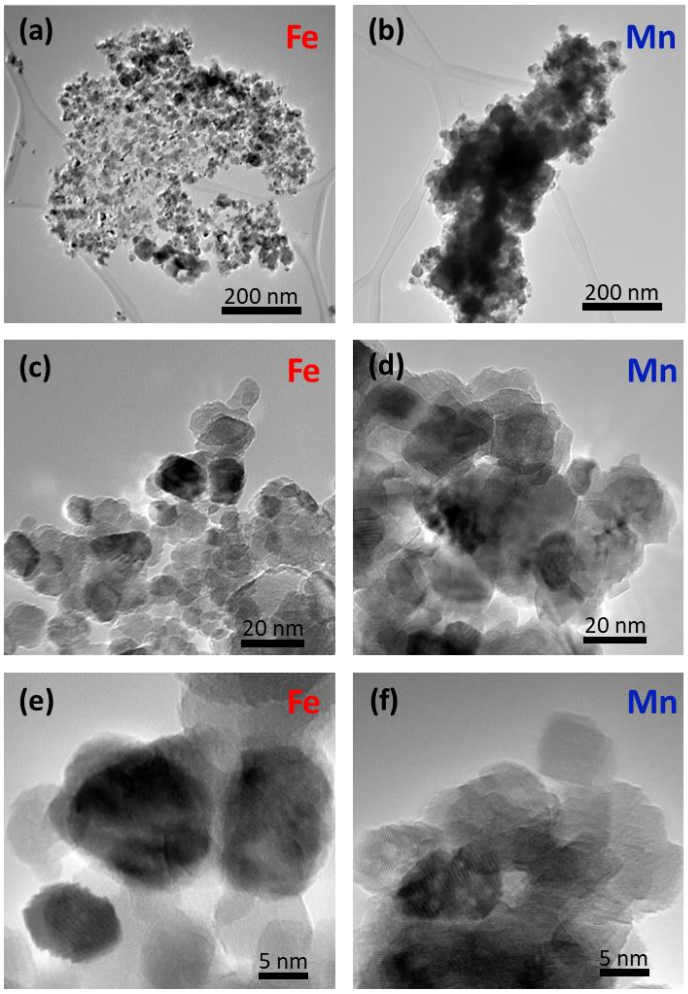

Figure S5: STEM images of the Fe- (a, c, e) and Mn- (b, d, f) doped NiO samples at different magnifications.

2.2 XPS and PXRD

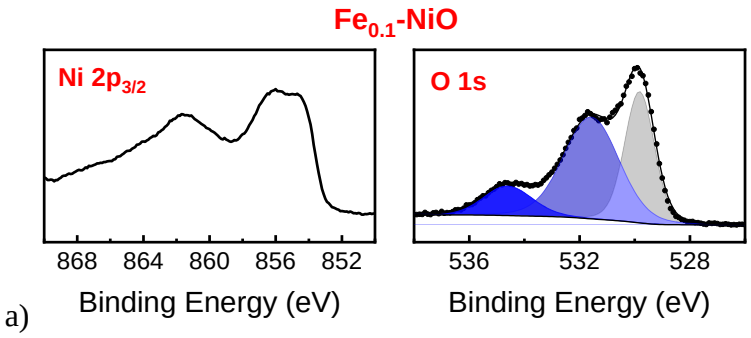

a)

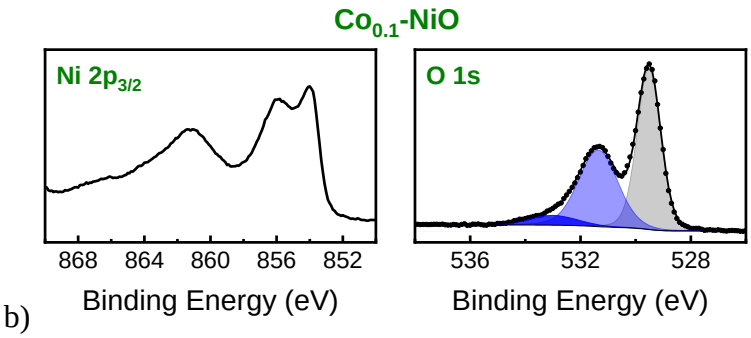

b)

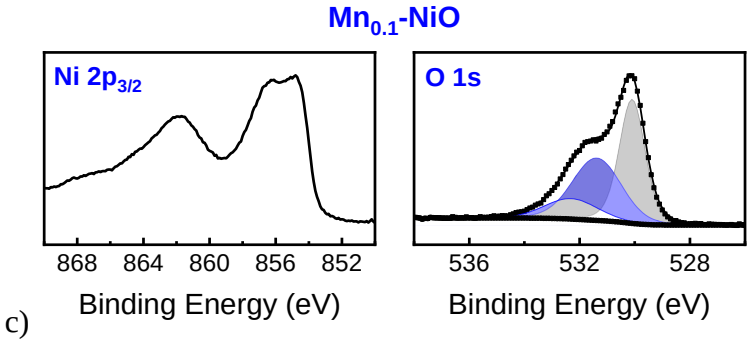

c)

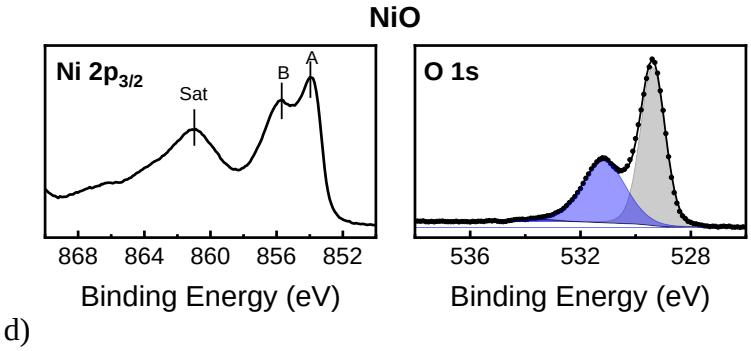

d)

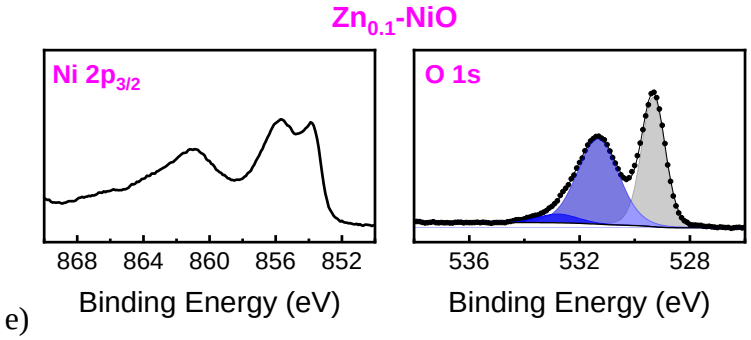

e)

Figure S6. XPS spectrum of Ni $2p_{3/2}$ (left) and O 1s (right) for $Fe_{0.1}$-NiO (a), $Co_{0.1}$-NiO (b), $Mn_{0.1}$-NiO (c), NiO (d), $Zn_{0.1}$-NiO (e).

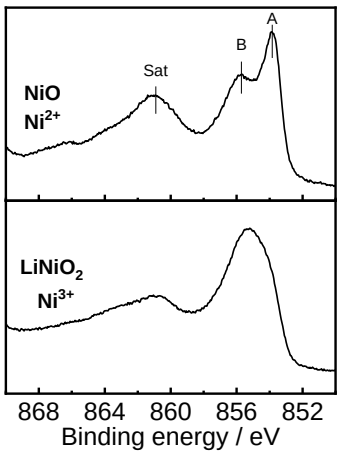

Figure S7. XPS in the Ni $2p_{3/2}$ Region of NiO and $LiNiO_2$ references.

The Ni $2p_{3/2}$ XPS spectrum is composed of complex features of multiple splitting, satellites and mixed Ni^{2+} and Ni^{3+} states. The two features marked as A and B in the Ni 2p spectra arise from many-electron excitation processes during photoemission, and should not be assigned to Ni^{2+} and Ni^{3+}. To estimate the oxidation state of Ni, we compared the Ni $2p_{3/2}$ lineshapes with those from reference samples, i.e. NiO representing Ni^{2+} and $LiNiO_2$ representing Ni^{3+}(Figure S7). Detailed comparison suggests that whereas Ni is mostly Ni^{2+} in the NiO electrode, the proportion of Ni^{3+} is increased in all doped NiO electrodes. However, due to the complexity of the Ni 2p XPS peak, a full quantification is difficult and often ambiguous.

The XPS in the O1s region is generally composed of three components: a low BE component associated to oxide lattice oxygen and two high BE components associated with hydroxy and carbonate surface species. Note that the proportion of these high BE components increase as the concentration of Ni (III) increases, which is something commonly seen in literature and associated with better electrode performances.

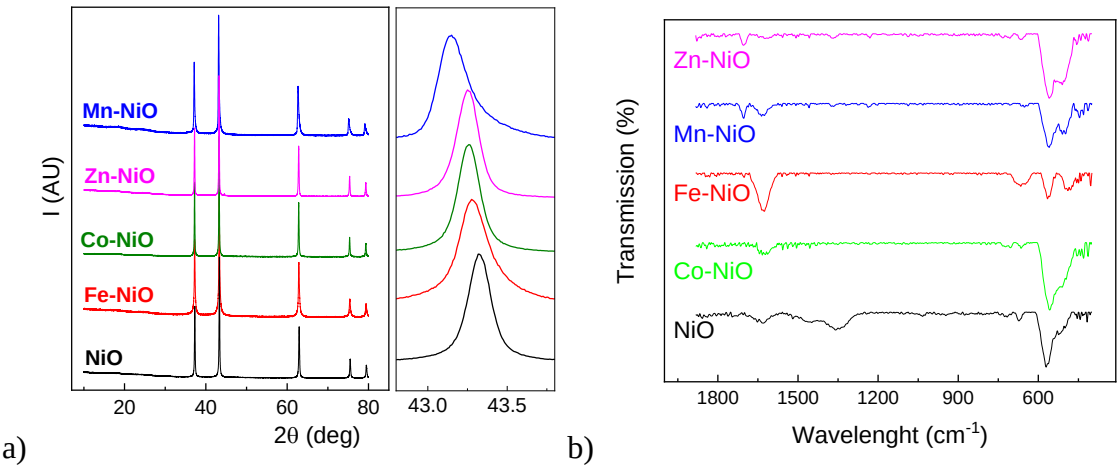

Figure S8. a) PXRD spectra of NiO and M-NiO (black = NiO, red = Fe, green = Co, blue = Mn and pink = Zn) with magnification of the peak at 43º in order to highlight the doping-induced peak shift and b) ATR-IR spectra of as-synthetized materials. A peak appearing at ~1630 cm^{-1} and corresponding to the bending mode of water molecules is very pronounced for $Fe_{0.1}$-NiO and $Co_{0.1}$-NiO, it becomes smaller for $Mn_{0.1}$-NiO and NiO, whereas it is negligible in the case of $Zn_{0.1}$-NiO.

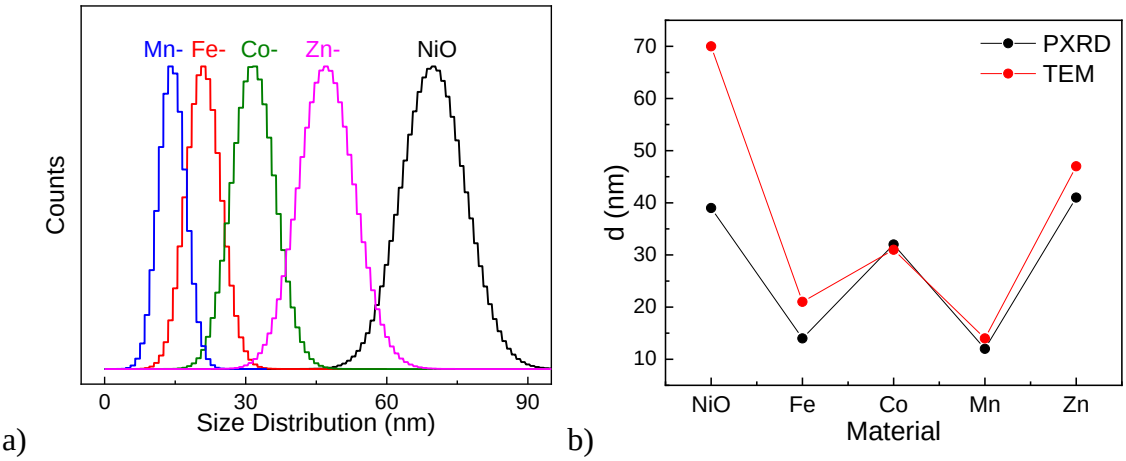

Figure S9. a) Size distribution for NiO and M-NiO materials obtained by TEM and b) comparison in the particle size obtained by the Scherrer equation from PXRD (black dots) and TEM sizes (red dots).

The samples were characterized by TEM microscopy (Figure S4) in order to rationalize the effect of doping on particle size. $Mn_{0.1}$-NiO and $Fe_{0.1}$-NiO show the smallest particle size, of ca. 14 and 21 nm, for $Co_{0.1}$-NiO and $Zn_{0.1}$-NiO a small increment to around 31

and 47 nm, respectively was observed, whereas NiO exhibits biggest particles of 70 nm (Figure S9a). The Scherrer equation used in the PXRD fitting gives the same results (Figure S9b), although for NiO the size is sub estimated in the fitting (ca. 40 nm).

2.3 EXAFS

Table S2: XANES parameters at the metal K-edge.

Sample	Oxidation State[1]	Dopant	K-Edge	E_0' (eV)[2]	$E_0^{1/2}$ (eV)[3]	Pre-edge Energy (eV)	Pre-edge Area
NiO	2.0	-	Ni	8343.8	8341.5	8332.1	0.057
$Zn_{0.1}$-NiO	2.0	Zn	Ni	8343.8	8341.5	8332.1	0.056
$Co_{0.1}$-NiO	2.0	Co	Ni	8343.8	8341.5	8332.1	0.057
$Fe_{0.1}$-NiO	2.0	Fe	Ni	8343.8	8341.5	8332.2	0.058
$Mn_{0.1}$-NiO	2.0	Mn	Ni	8343.8	8341.5	8332.1	0.059
$Co_{0.1}$-NiO	2.0	Co	Co	7721.8	7718.8	7710.2	0.09
$Fe_{0.1}$-NiO	3.0	Fe	Fe	7121.7	7123.2	7113.3	0.16
$Mn_{0.1}$-NiO	3.1	Mn	Mn	6547.9	6551.1	6540.7	0.13

1) Oxidation state values were taken from comparison with: Inorg. Chem. 1991, 30, 920(Ni); PLoS One 2016, 11 (7), 1(Co K-edge); J. Am. Chem. Soc. 1997, 119, 6297 (Fe K-edge), J. Phys. Chem. C 2007, 111, 749 (Mn K-edge)
2) E0' values at the Ni and Co K-edges were taken as the maximum infection point of the first derivative, for Fe and Mn K-edges was taken as the first maximum of the first derivative
3) E01/2 values were taken at the half-height ie. 0.5 normalized intensity units of the rising edge

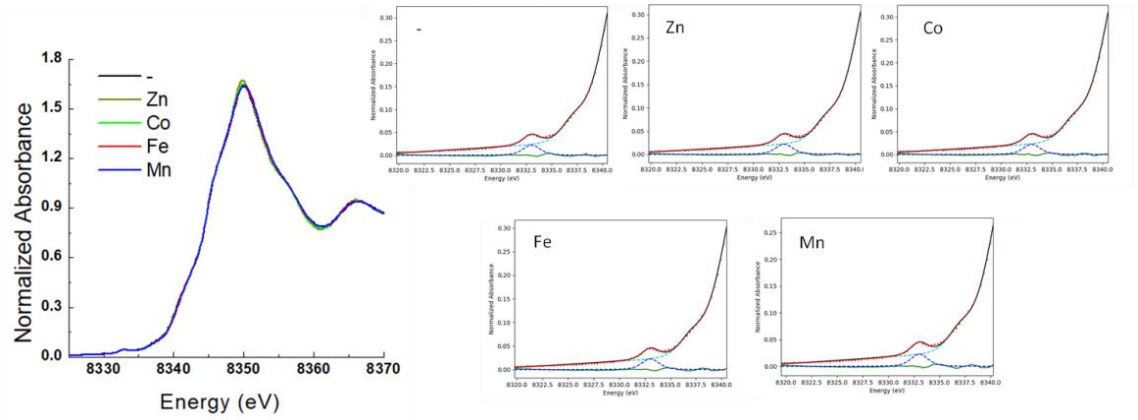

Figure S10. Ni K-edge XANES spectra and pre-edge fits of neat (-) and doped (Zn, Co, Fe, Mn) NiO.

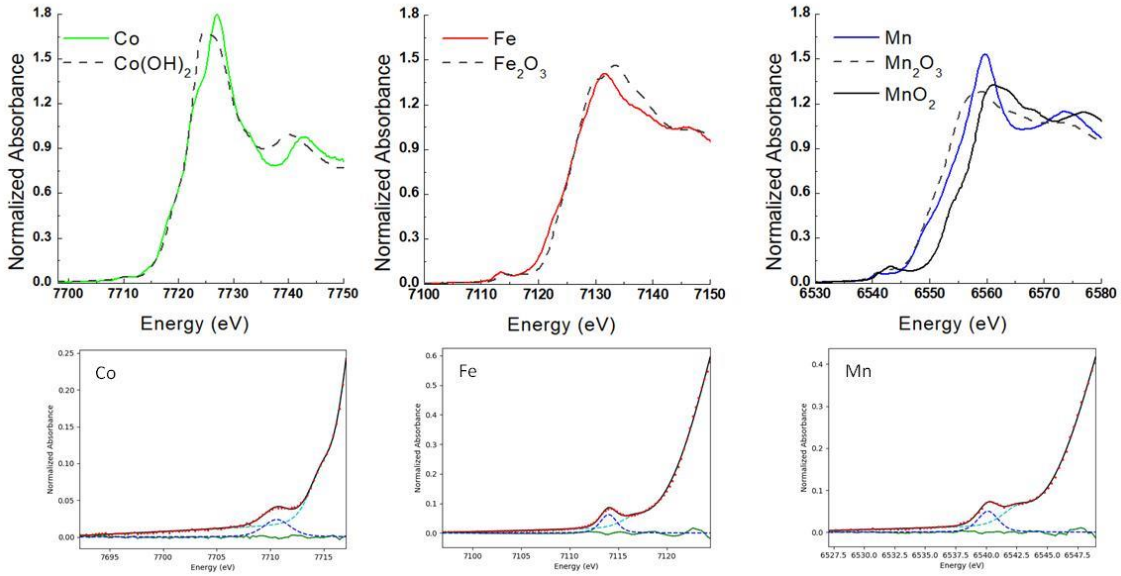

Figure S11. XANES spectra and pre-edge fits of Co-, Fe- and Mn- doped NiO at the dopant metal K-edge, along with appropriate reference spectra ($Co(OH)_2$, Fe_2O_3, Mn_2O_3 and MnO_2).

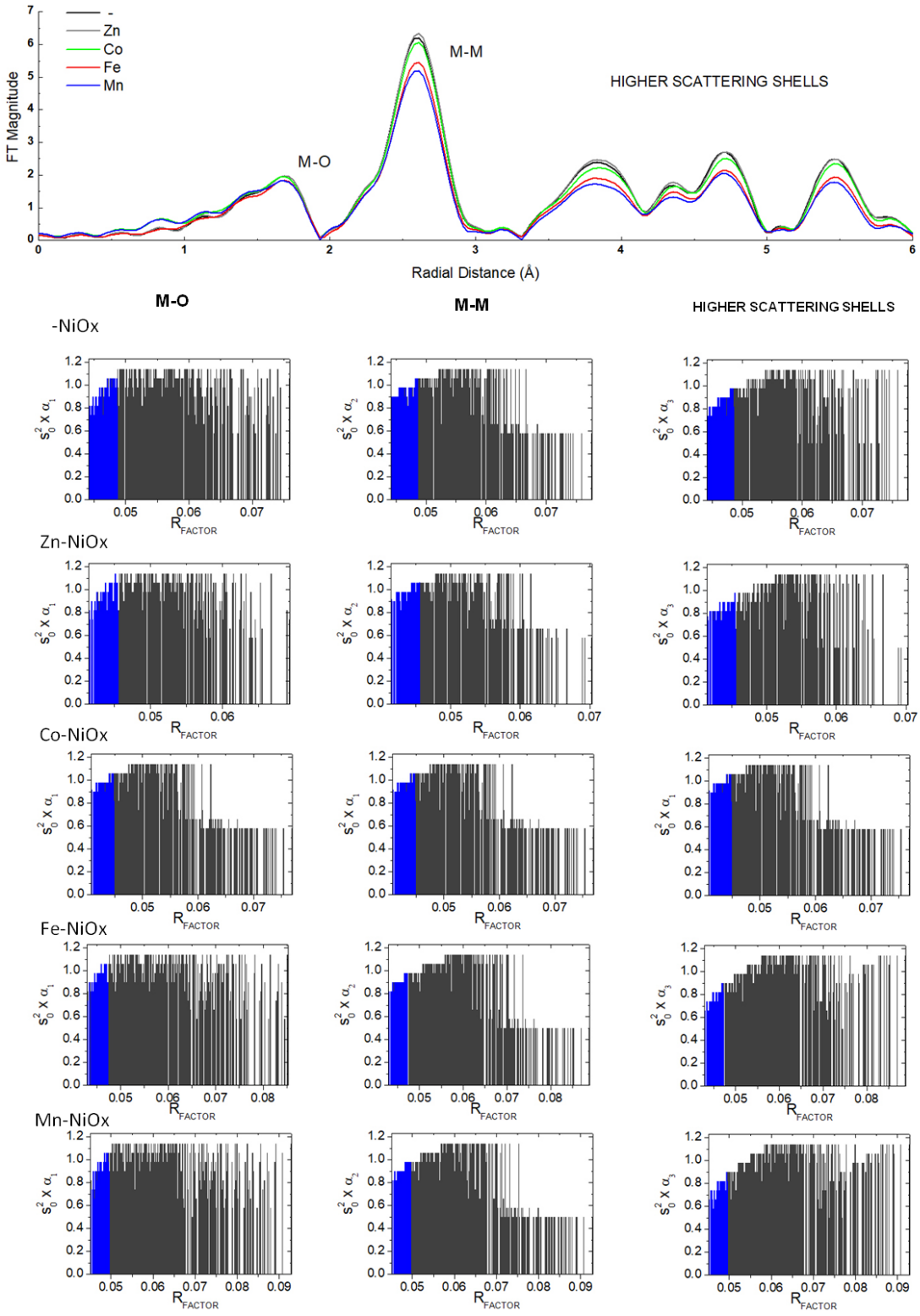

Figure S12. Grid search EXAFS screening of NiO species at the Ni K-edge showing the goodness of fit versus variation in coordination number in terms of $S_0^2 * a_x *$(theoretical path degeneracy). Bars in grey represent filtered fits ensuring ranges for Δr_{eff} of +/- 0.10

Å, σ^2 0.001 to 0.012 Å^2 and ΔE_0 of +/- 12 eV. Bars in blue represent the top 10% of fits relative to the lowest R_{FACTOR}.

Table S3. Summary of EXAFS analysis at the Ni K-edge. Multi (k^2, k^3)-weighted fits carried out in r-space over a k-range of 3-15 Å using a Hanning window (dk 1), and an S_0 = 0.9. Bond distances and disorder parameters (Δr_{eff} and σ^2) were allowed to float having initial values of 0.0 Å and 0.003 Å^2 respectively. A universal E_0 was applied to all paths with the initial guess ΔE_0 = 0 eV. Coordination numbers for the final model fits was determined from the average of the top 10% fits from the grid search screening. Precision error for the coordination number is in the 10% - 15% range.

Sample		-NiOx	Zn-NiOx	Co-NiOx	Fe-NiOx	Mn-NiOx
Δk		3.0-15.0	3.0-15.0	3.0-15.0	3.0-15.0	3.0-15.0
Δr		1.0-6.0	1.0-6.0	1.0-6.0	1.0-6.0	1.0-6.0
R_{FACTOR}		0.0444	0.0416	0.0399	0.0422	0.0451
χ^2_ν		136.6	124.9	166.2	101.2	117.0
ΔE0		-2.51 +/- 0.69	-2.62 +/- 0.67	-3.06 +/- 0.66	-2.62 +/- 0.68	-2.59 +/- 0.71
M-O-M	N	5.89	6.09	6.09	6.03	6.13
	r (Å)	2.066 +/- 0.01	2.07 +/- 0.01	2.069 +/- 0.0098	2.068 +/- 0.0097	2.066 +/- 0.0099
	σ^2 (Å^2)	0.003612 +/- 0.0013	0.003733 +/- 0.0013	0.004078 +/- 0.0013	0.004415 +/- 0.0012	0.004671 +/- 0.0013
M-Ni-M	N	11.92	12.26	12.18	11.06	11.35
	r (Å)	2.945 +/- 0.0039	2.95 +/- 0.0038	2.951 +/- 0.0037	2.95 +/- 0.0039	2.949 +/- 0.0042
	σ^2 (Å^2)	0.00284 +/- 0.00025	0.00285 +/- 0.00024	0.003052 +/- 0.00024	0.003178 +/- 0.00024	0.003626 +/- 0.00026
M-O-M	N	6.96	6.94	6.80	6.23	6.03
	r (Å)	3.595 +/- 0.01	3.599 +/- 0.01	3.597 +/- 0.0098	3.596 +/- 0.0097	3.594 +/- 0.0099
	σ^2 (Å^2)	0.003386 +/- 0.0003	0.003261 +/- 0.00029	0.003564 +/- 0.0003	0.00398 +/- 0.00033	0.004257 +/- 0.00036
M-Ni-M	N	5.22	5.20	5.10	4.68	4.52
	r (Å)	4.168 +/- 0.0039	4.173 +/- 0.0038	4.174 +/- 0.0037	4.173 +/- 0.0039	4.172 +/- 0.0042
	σ^2 (Å^2)	0.003386 +/- 0.0003	0.003261 +/- 0.00029	0.003564 +/- 0.0003	0.00398 +/- 0.00033	0.004257 +/- 0.00036
M-Ni-O-M	N	10.43	10.41	10.20	9.35	9.04
	r (Å)	4.168 +/- 0.0039	4.173 +/- 0.0038	4.174 +/- 0.0037	4.173 +/- 0.0039	4.172 +/- 0.0042
	σ^2 (Å^2)	0.003386 +/- 0.0003	0.003261 +/- 0.00029	0.003564 +/- 0.0003	0.00398 +/- 0.00033	0.004257 +/- 0.00036
M-O-Ni-O-M	N	5.22	5.20	5.10	4.68	4.52
	r (Å)	4.168 +/- 0.0039	4.173 +/- 0.0038	4.174 +/- 0.0037	4.173 +/- 0.0039	4.172 +/- 0.0042
	σ^2 (Å^2)	0.003386 +/- 0.0003	0.003261 +/- 0.00029	0.003564 +/- 0.0003	0.00398 +/- 0.00033	0.004257 +/- 0.00036
M-O-M	N	20.87	20.81	20.40	18.70	18.08
	r (Å)	4.647 +/- 0.01	4.651 +/- 0.01	4.65 +/- 0.0098	4.649 +/- 0.0097	4.647 +/- 0.0099
	σ^2 (Å^2)	0.003386 +/- 0.0003	0.003261 +/- 0.00029	0.003564 +/- 0.0003	0.00398 +/- 0.00033	0.004257 +/- 0.00036
M-Ni-M	N	20.87	20.81	20.40	18.70	18.08
	r (Å)	5.107 +/- 0.0039	5.112 +/- 0.0038	5.113 +/- 0.0037	5.112 +/- 0.0039	5.111 +/- 0.0042
	σ^2 (Å^2)	0.003386 +/- 0.0003	0.003261 +/- 0.00029	0.003564 +/- 0.0003	0.00398 +/- 0.00033	0.004257 +/- 0.00036
M-Ni-Ni-M	N	20.87	20.81	20.40	18.70	18.08
	r (Å)	5.898 +/- 0.0039	5.903 +/- 0.0038	5.904 +/- 0.0037	5.903 +/- 0.0039	5.902 +/- 0.0042
	σ^2 (Å^2)	0.003386 +/- 0.0003	0.003261 +/- 0.00029	0.003564 +/- 0.0003	0.00398 +/- 0.00033	0.004257 +/- 0.00036
M-Ni-Ni-Ni-M	N	10.43	10.41	10.20	9.35	9.04
	r (Å)	5.898 +/- 0.0039	5.903 +/- 0.0038	5.904 +/- 0.0037	5.903 +/- 0.0039	5.902 +/- 0.0042
	σ^2 (Å^2)	0.003386 +/- 0.0003	0.003261 +/- 0.00029	0.003564 +/- 0.0003	0.00398 +/- 0.00033	0.004257 +/- 0.00036

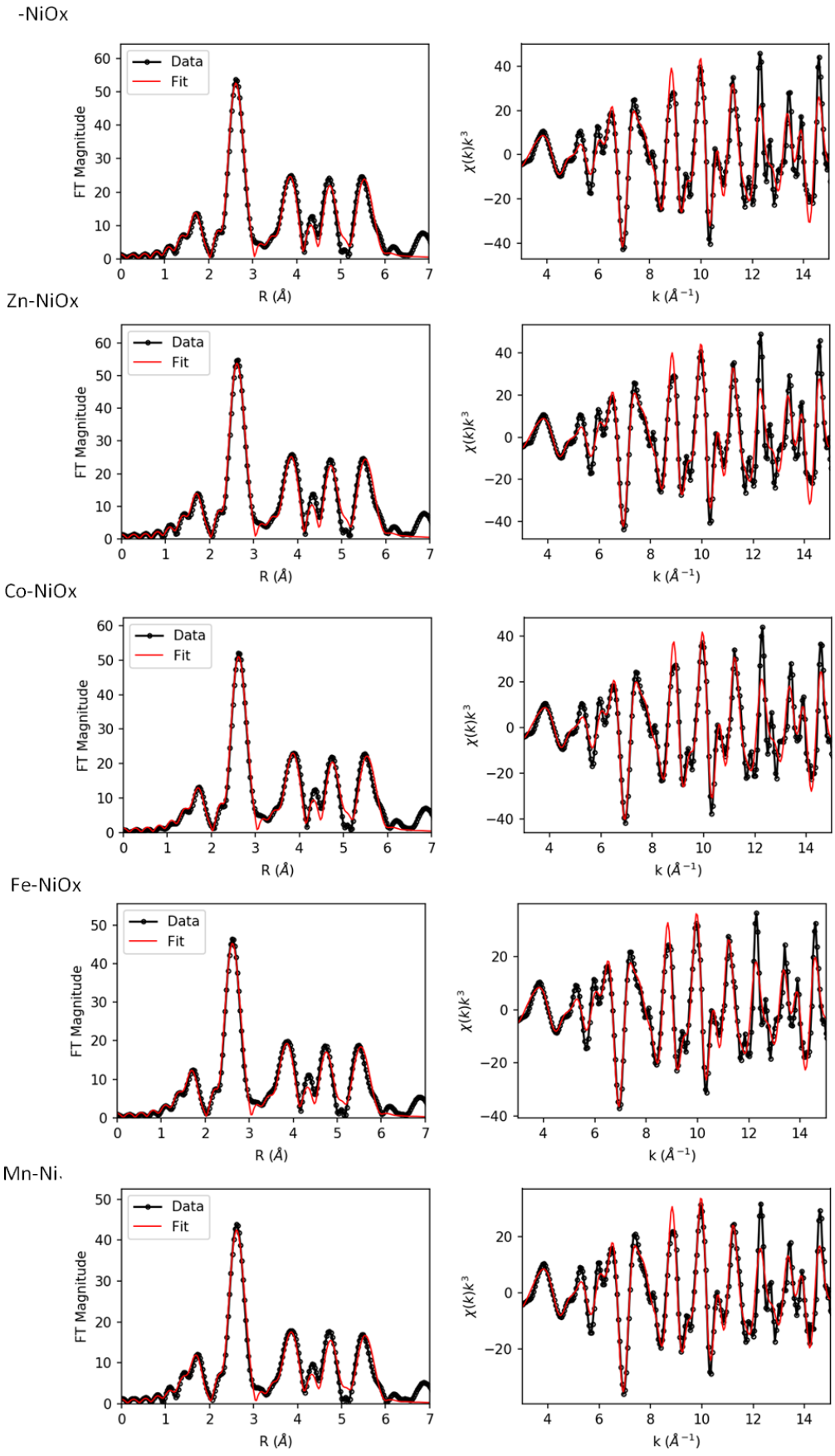

Figure S13. EXAFS Fits from analysis at the Ni K-edge, presented in Table S3.

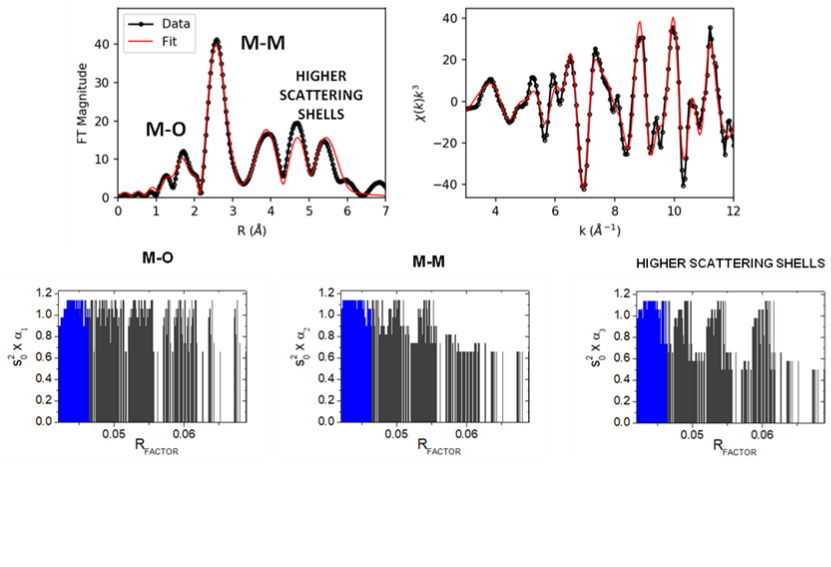

Sample		Co-NiOx
Δk		3.0-12.0
Δr		1.0-6.0
R_{FACTOR}		0.0415
χ^2_v		121.4
ΔE0		-3.513 +/- 0.85
M-O-M	N	5.67
	r (Å)	2.064 +/- 0.013
	σ^2 (Å^2)	0.005074 +/- 0.0019
M-Ni-M	N	12.95
	r (Å)	2.949 +/- 0.0056
	σ^2 (Å^2)	0.003763 +/- 0.00035
M-O-M	N	7.87
	r (Å)	3.593 +/- 0.013
	σ^2 (Å^2)	0.004666 +/- 0.00046
M-Ni-M	N	5.90
	r (Å)	4.172 +/- 0.0056
	σ^2 (Å^2)	0.004666 +/- 0.00046
M-Ni-O-M	N	11.80
	r (Å)	4.172 +/- 0.0056
	σ^2 (Å^2)	0.004666 +/- 0.00046
M-O-Ni-O-M	N	5.90
	r (Å)	4.172 +/- 0.0056
	σ^2 (Å^2)	0.004666 +/- 0.00046
M-O-M	N	23.61
	r (Å)	4.645 +/- 0.013
	σ^2 (Å^2)	0.004666 +/- 0.00046
M-Ni-M	N	23.61
	r (Å)	5.111 +/- 0.0056
	σ^2 (Å^2)	0.004666 +/- 0.00046
M-Ni-Ni-M	N	23.61
	r (Å)	5.902 +/- 0.0056
	σ^2 (Å^2)	0.004666 +/- 0.00046
M-Ni-Ni-Ni-M	N	11.80
	r (Å)	5.902 +/- 0.0056
	σ^2 (Å^2)	0.004666 +/- 0.00046

Figure S14. Summary of EXAFS analysis of $Co_{0.1}$-NiO at the Co K-edge. Multi (k^2, k^3)-weighted fits carried out in r-space over a k-range of 3-12 Å using a Hanning window (dk 1), and an S_0 = 0.95 was chosen. Bond distances and disorder parameters (Δr_{eff} and σ^2) were allowed to float having initial values of 0.0 Å and 0.003 Å^2 respectivel. A universal E_0 was applied to all paths with the initial guess ΔE_0 = 0 eV. Coordination numbers for the final model fits were determined from the average of the top 10% fits from the grid search screening. Precision error for the coordination number is in the 10% - 15% range: (TOP LEFT) Final Fit; (BOTTOM LEFT) Grid search screening of coordination numbers using the same procedure as in Figure S12; (RIGHT) Final fit metrics.

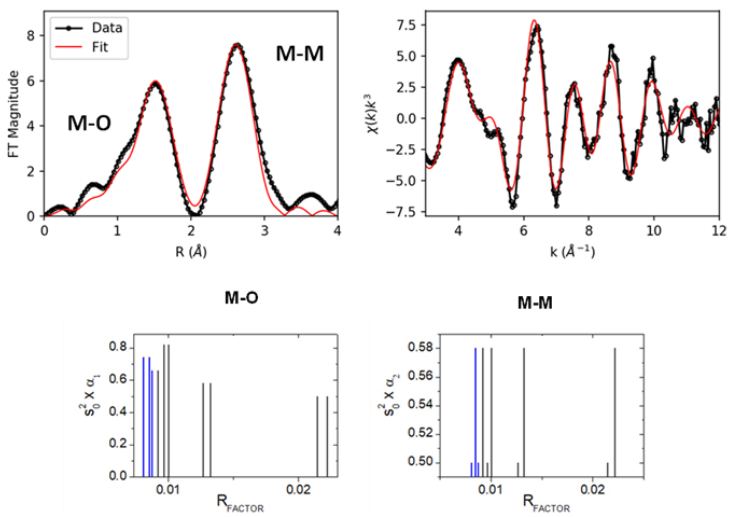

Sample		Fe-NiOx
Δk		3.0-12.0
Δr		1.0-3.0
R_{FACTOR}		0.0079
χ^2_ν		15.3
ΔE0		-2.118 +/- 0.85
M-O-M	N	4.75
	r (Å)	1.982 +/- 0.0074
	σ^2 (Å^2)	0.00912 +/- 0.00069
M-Ni-M	N	7.02
	r (Å)	2.994 +/- 0.0067
	σ^2 (Å^2)	0.01089 +/- 0.00044

Figure S15. Summary of EXAFS analysis of $Fe_{0.1}$-NiO at the Fe K-edge. Multi (k^2, k^3)-weighted fits carried out in r-space over a k-range of 3-12 Å using a Hanning window (dk 1), and an $S_0 = 0.90$ was chosen. Bond distances and disorder parameters (Δr_{eff} and σ^2) were allowed to float having initial values of 0.0 Å and 0.003 Å^2 respectively. A universal E_0 was applied to all paths with the initial guess $\Delta E_0 = 0$ eV. Coordination numbers for the final model fits were determined from the average of the top 10% fits from the grid search screening. Precision error for the coordination number is in the 10% - 15% range: (TOP LEFT) Final Fit; (BOTTOM LEFT) Grid search screening of coordination numbers using the same procedure as in Figure S12; (RIGHT) Final fit metrics.

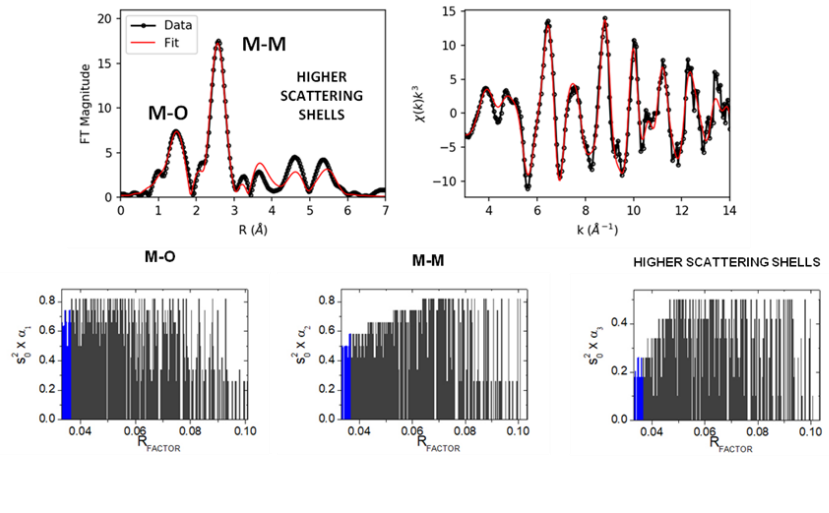

Sample		Mn-NiOx
Δk		3.0-14.0
Δr		1.0-6.0
R_{FACTOR}		0.0339
χ^2_ν		19.7
ΔE0		-9.027 +/- 0.86
M-O-M	N	4.24
	r (Å)	1.909 +/- 0.0069
	σ^2 (Å^2)	0.005491 +/- 0.00072
M-Ni-M	N	6.56
	r (Å)	2.945 +/- 0.0092
	σ^2 (Å^2)	0.005087 +/- 0.00026
M-Ni-O-M	N	2.72
	r (Å)	4.164 +/- 0.0092
	σ^2 (Å^2)	0.005665 +/- 0.00074
M-O-Ni-O-M	N	0.00
	r (Å)	4.164 +/- 0.0092
	σ^2 (Å^2)	0.005665 +/- 0.00074
M-O-M	N	5.44
	r (Å)	4.656 +/- 0.0092
	σ^2 (Å^2)	0.005665 +/- 0.00074
M-Ni-M	N	5.44
	r (Å)	5.1 +/- 0.0092
	σ^2 (Å^2)	0.005665 +/- 0.00074
M-Ni-Ni-M	N	5.44
	r (Å)	5.889 +/- 0.0092
	σ^2 (Å^2)	0.005665 +/- 0.00074
M-Ni-Ni-Ni-M	N	2.72
	r (Å)	5.889 +/- 0.0092
	σ^2 (Å^2)	0.005665 +/- 0.00074

Figure S16. Summary of EXAFS analysis of $Mn_{0.1}$-NiO at the Mn K-edge. Multi (k^2, k^3)-weighted fits carried out in r-space over a k-range of 3-12 Å using a Hanning window (dk 1), and an $S_0 = 0.90$ was chosen. Bond distances and disorder parameters (Δr_{eff} and σ^2) were allowed to float having initial values of 0.0 Å and 0.003 Å^2 respectively. A universal E_0 was applied to all paths with the initial guess $\Delta E_0 = 0$ eV. Coordination numbers for the final model fits were determined from the average of the top 10% fits from the grid search screening. Precision error for the coordination number is in the 10% - 15% range: (TOP LEFT) Final Fit; (BOTTOM LEFT) Grid search screening of coordination numbers using the same procedure as in Figure S12; (RIGHT) Final fit metrics.

3. Electrochemistry

3.1 (M)-NiO/NF

3.3.1 Catalyst loading optimization.

Before running electrochemical tests, the catalyst loading has been optimized by changing the concentration of the combustion mixture in the range between 0.05 M to 2 M (Figure S17a), finding that the best activity was obtained for the combustion mixture 0.5 M (Figure S17b and S17c).

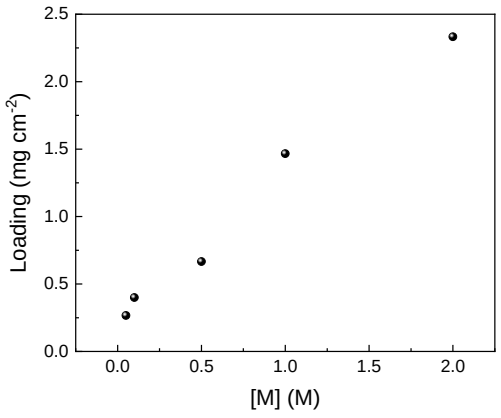

a)

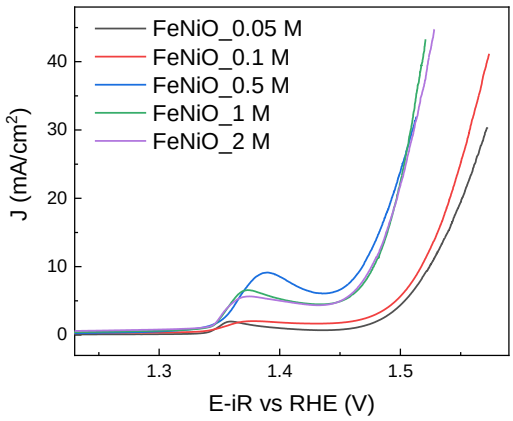

b)

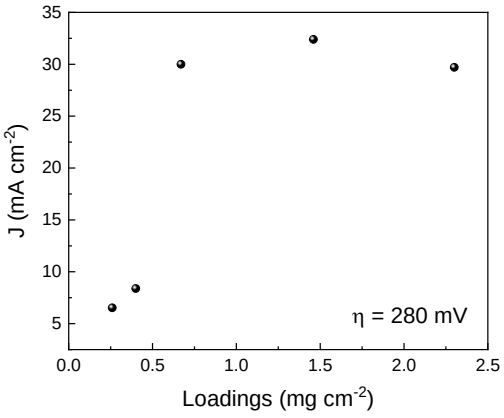

c)

Figure S17. (a) Effect of the concentration of the metal precursor in the combustion mixture on the amount of deposited material. (b) LSV comparison and trend of the current (c) as a function of the loading.

The amount of material deposited increases linearly with the concentration as shown in the Figure S17. For loadings as low as 0.2 – 0.4 mg/cm^2, the activity is low if compared to the standard loading used in the rest of the work (0.67 mg/cm^2), probably because not all the NF is fully covered by the catalyst and there is still room to accommodate the catalyst particles ensuring a good electrical contact with the support. However, no major differences have been observed by increasing the loading from 0.67 mg/cm^2 to 2.3 mg/cm^2, suggesting that having thicker film does not improve the catalytic performances, owing to lower exposure of active sites to the electrolyte.

3.1.2 Blank experiments

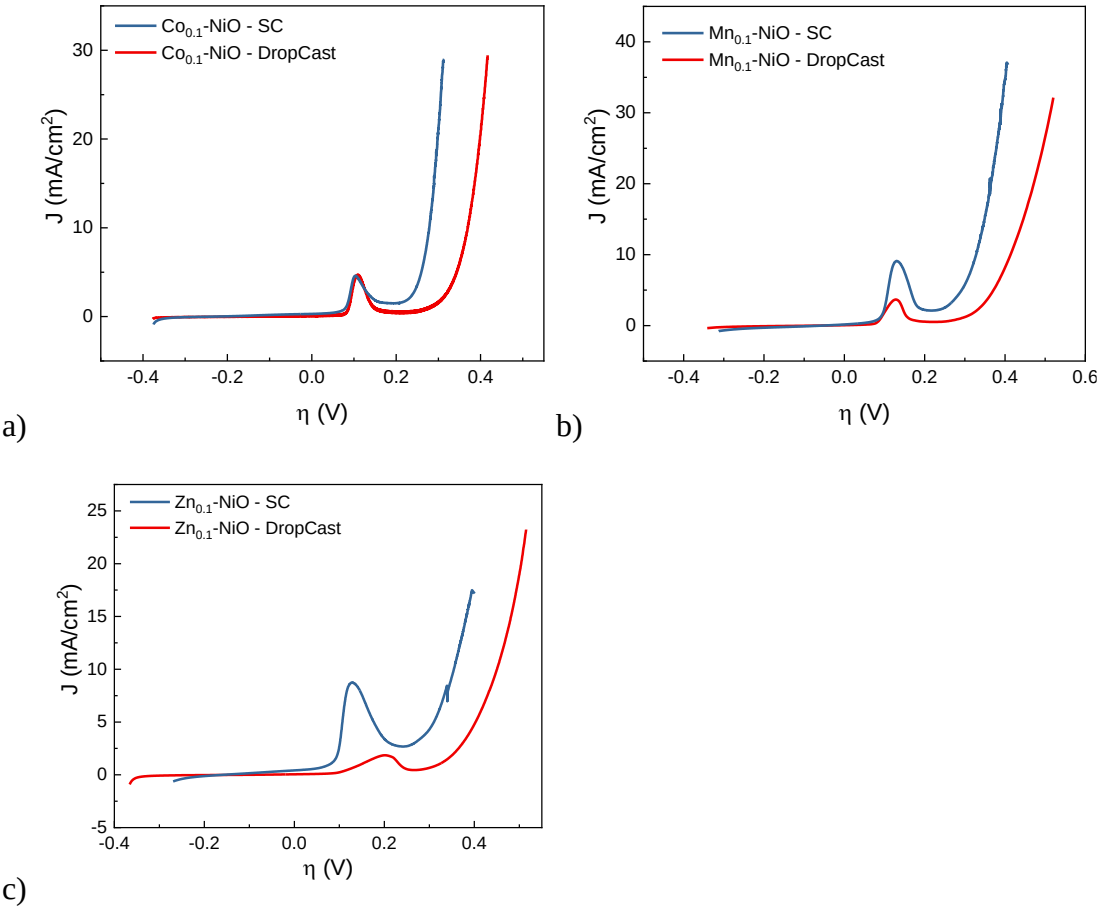

Figure S18. Beneficial effect of self-supporting M-NiO catalysts (Co in panel a), Mn in panel b) and Zn in panel c)) on NF (blue LSV) over drop casting the same material on NF (red LSV).

a) 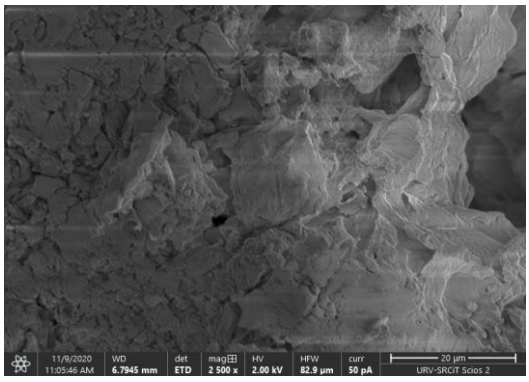 b) 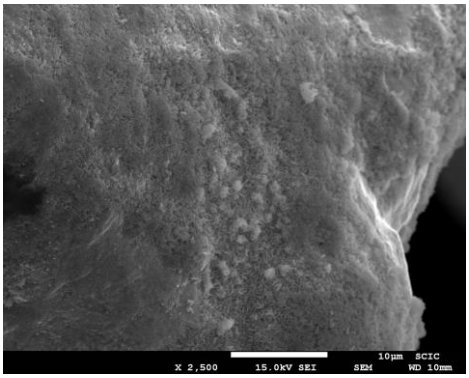

Figure S19. SEM micrographs showing the morphological differences between $Fe_{0.1}NiO$ prepared by TND (a) and SC (b).

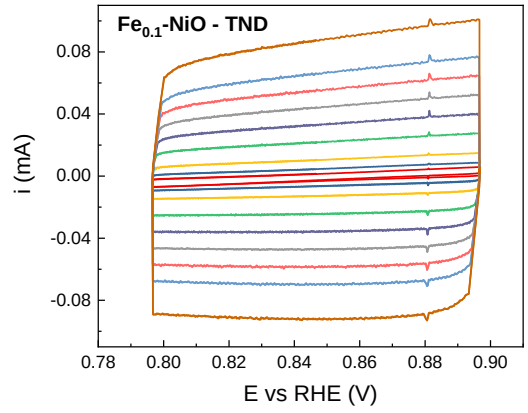

a)

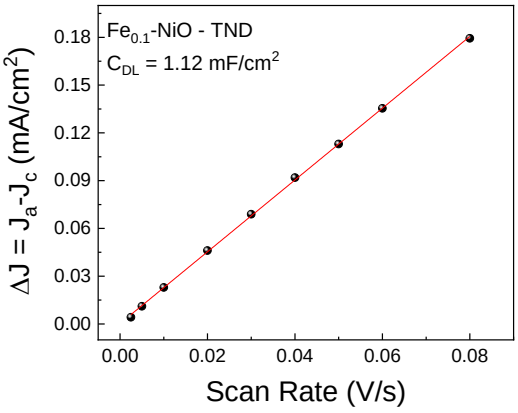

b)

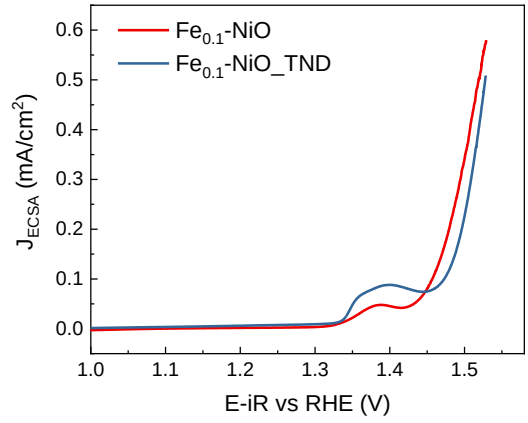

c)

Figure S20. Evaluation of the ECSA for $Fe_{0.1}$-NiO (TND) (panels (a) and (b)) and ECSA-normalized current for TND (blue) and SC (red) prepared $Fe_{0.1}$-NiO samples.

3.1.3 Electrochemical Impedance Spectroscopy (EIS).

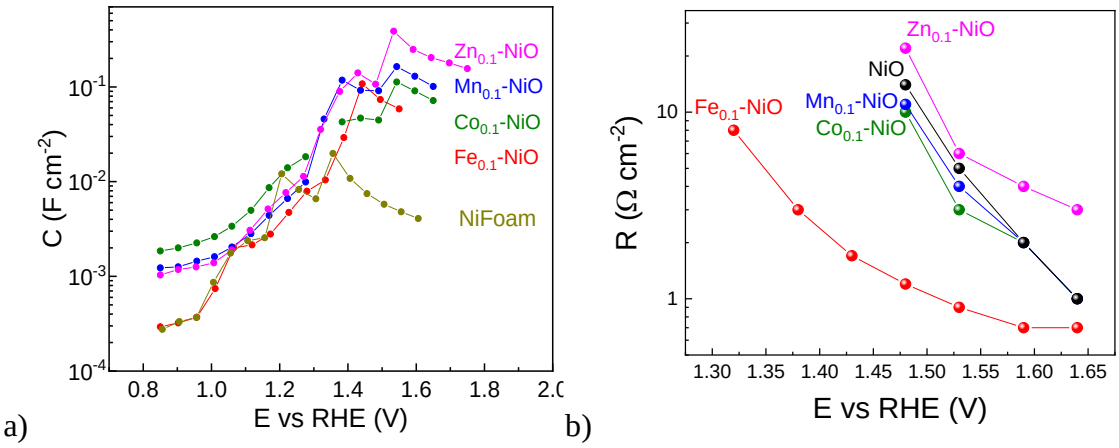

Figure S21. Evolution of the capacitance (a) and the resistance (b) as a function of applied potential for M-NiO@NF in comparison with reference NF.

Table S4. Summary of capacitance and charge-transfer resistance values at different potential applied for NiO@NF and M-NiO@NF.

E vs RHE	$Fe_{0.1}$-NiO		$Co_{0.1}$-NiO		$Mn_{0.1}$-NiO	
(V)	C (mF/cm^{-2})	R (Ω/cm^{-2})	C (mF/cm^{-2})	R (Ω/cm^{-2})	C (mF/cm^{-2})	R (Ω/cm^{-2})
0.85	10		2		1	
0.90	4		2		1	
0.96	7		2		1	
1.01	6		3		2	
1.06	2		3		2	
1.11	3		5		3	
1.17	5		9		4	
1.22	7		14		7	
1.27	10		18		10	
1.32	49	8	-		46	
1.38	55	3	43		118	
1.43	60	1.7	47		92	
1.48	129	1.2	45	10	91	11
1.53	81	0.9	113	4	164	5
1.59	51	0.7	91	2	130	2
1.64	39	0.7	72	1	101	1

E vs RHE	NiO		$Zn_{0.1}$-NiO	
(V)	C (mF/cm^{-2})	R (Ω/cm^{-2})	C (mF/cm^{-2})	R (Ω/cm^{-2})
0.85	0.3		1	
0.90	0.3		2	
0.96	0.4		3	
1.01	1		7	
1.06	2		11	
1.11	2		-	
1.17	3		70	
1.22	12		50	
1.27	8		38	
1.32	7		32	
1.38	20		34	
1.43	11		1	
1.48	7	14	2	22
1.53	6	3	3	6
1.59	5	2	7	4
1.64	4	1	11	3

3.1.4 Faradaic Yields.

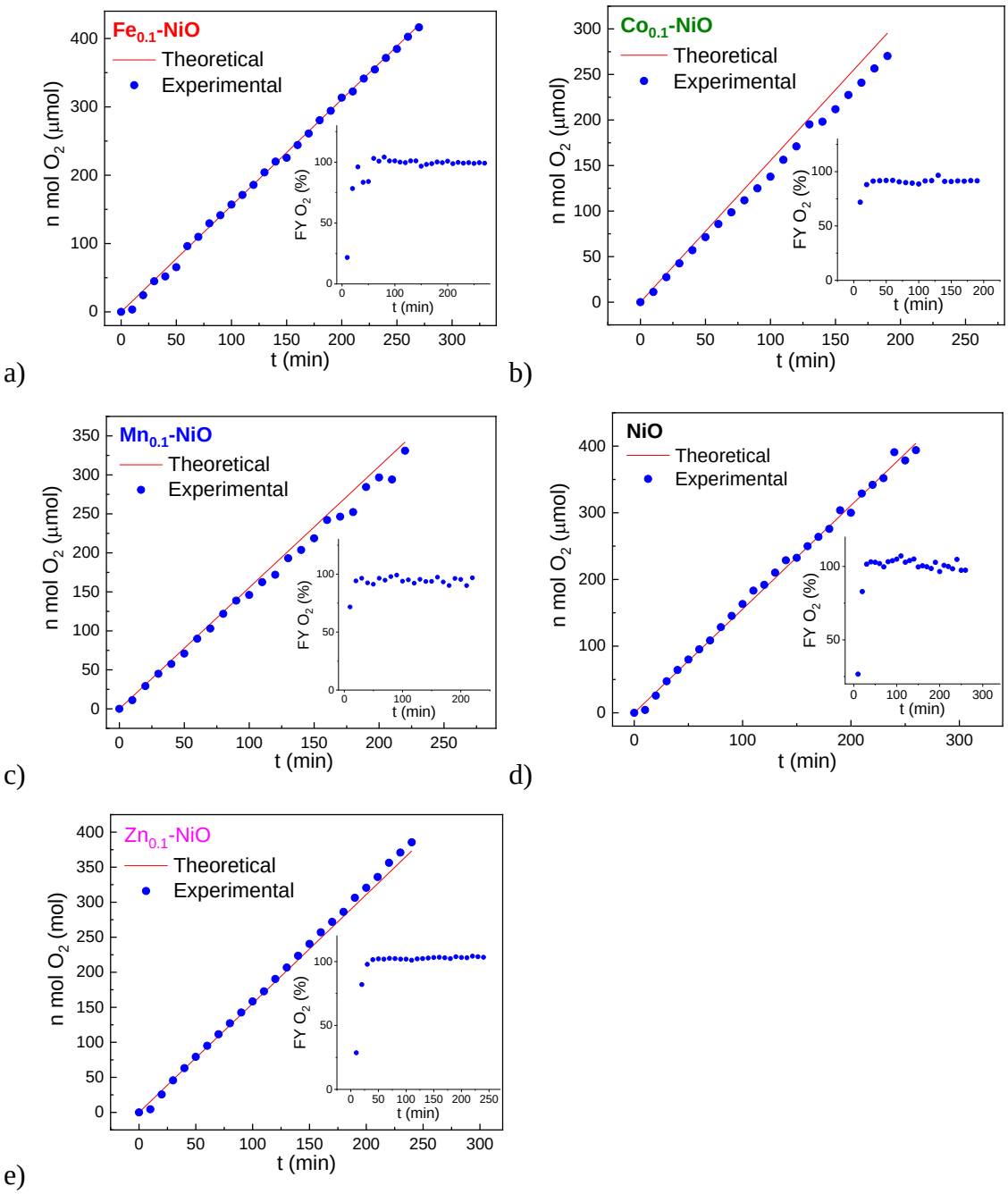

Figure S22. Determination of O_2 production during CP experiment (5 hours at 10 mA/cm^2) by means of on-line GC for $Fe_{0.1}$-NiO (a), $Co_{0.1}$-NiO (b), $Mn_{0.1}$-NiO (c), NiO (d) and $Zn_{0.1}$-NiO (e). During the experiments, the sampling time was 10 minutes with a flow rate of 30 mL/min. The inset of each graph represents the Faradaic Yield calculated by the ratio between experimental moles of O_2 detected and theoretical ones, as a function of time.

3.1.5 Determination of electrochemical surface area (ECSA).

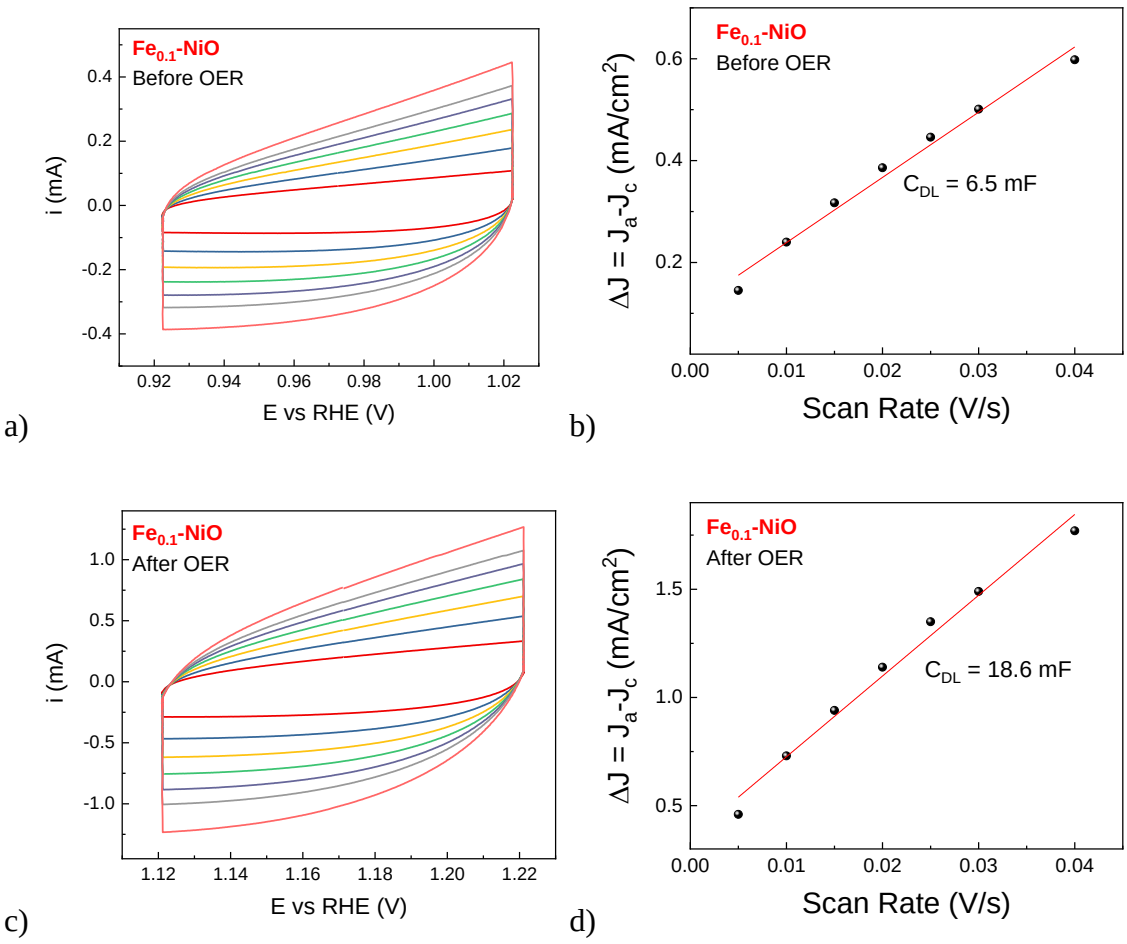

Figure S23. Determination of double-layer capacitance for $Fe_{0.1}$-NiO before (a and b) and after (c and d) OER.

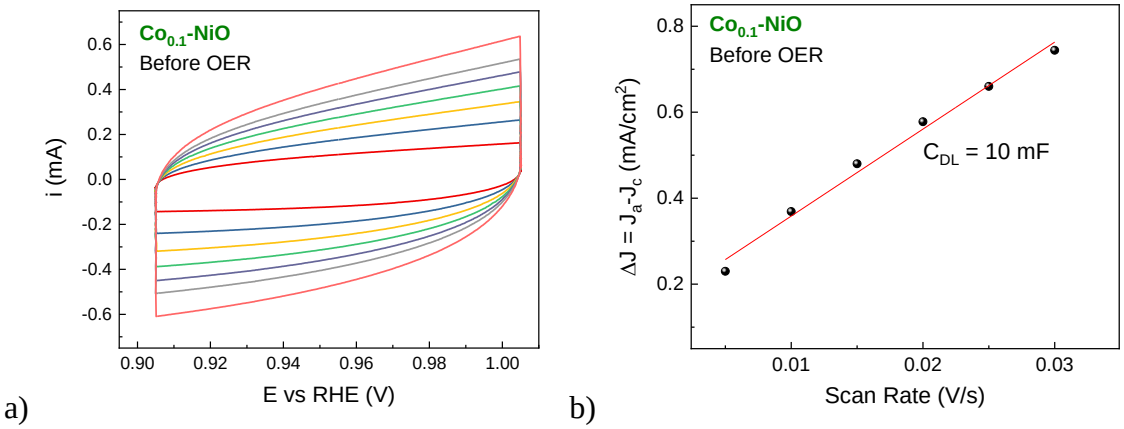

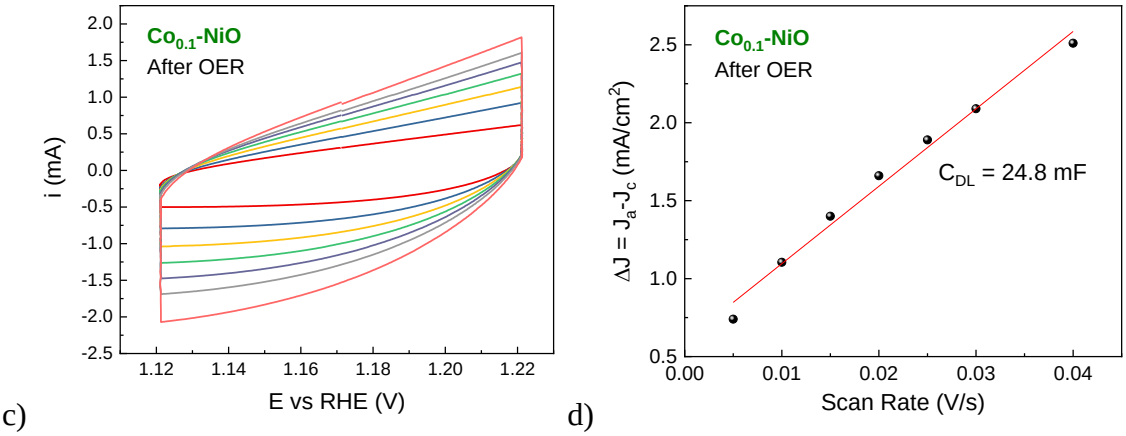

c) d)

Figure S24. Determination of double-layer capacitance for $Co_{0.1}$-NiO before (a and b) and after (c and d) OER.

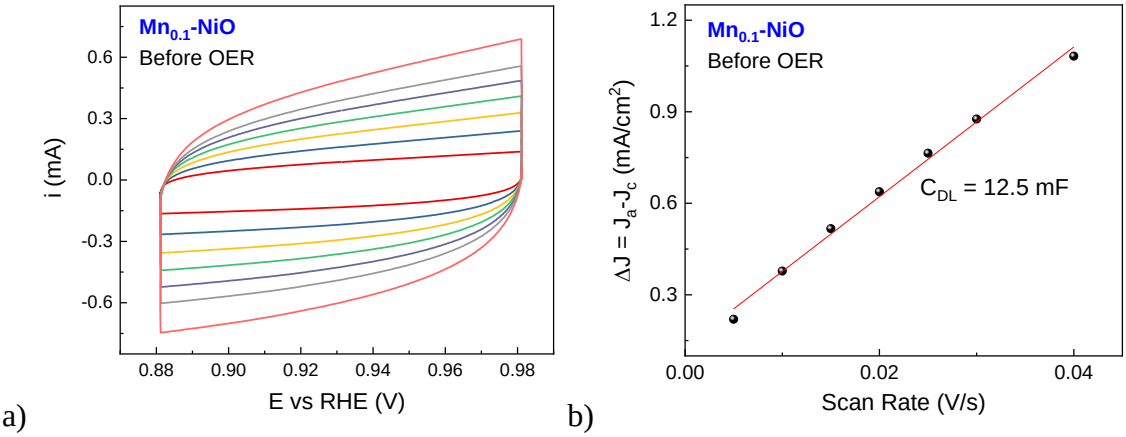

a) b)

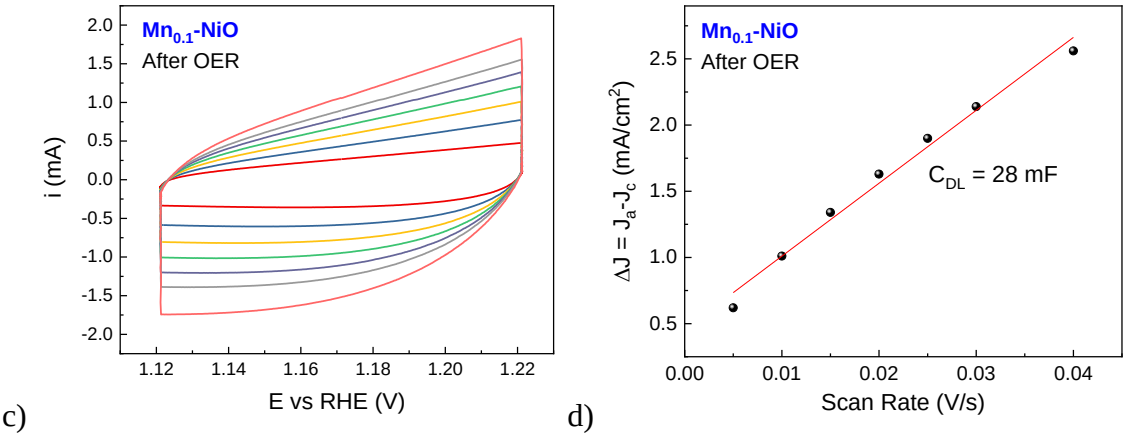

c) d)

Figure S25. Determination of double-layer capacitance for $Mn_{0.1}$-NiO before (a and b) and after (c and d) OER.

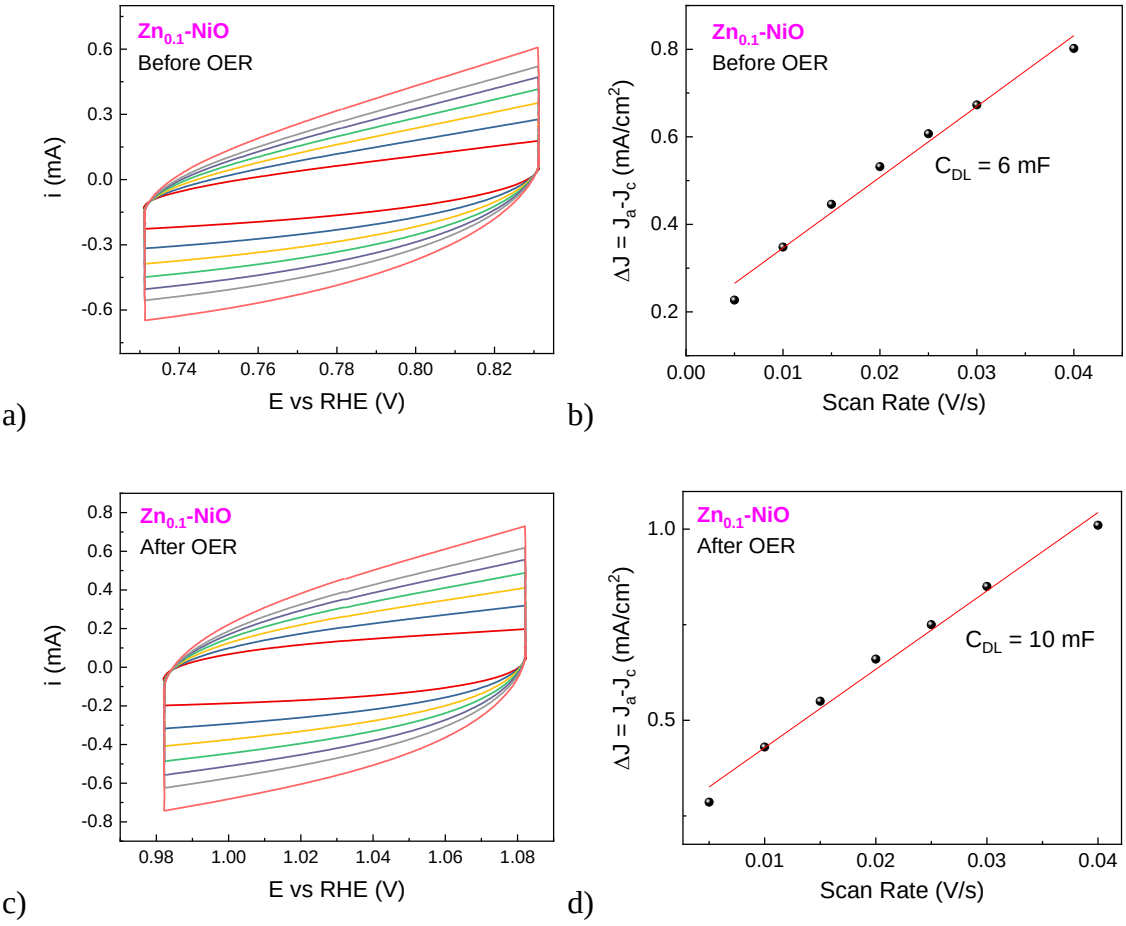

Figure S26. Determination of double-layer capacitance for $Zn_{0.1}$-NiO before (a and b) and after (c and d) OER.

Table S5. Summary of ECSA values obtained before and after OER.

Material	Before OER		After OER	
	C_{DL} (mF)	ECSA (cm^2)	C_{DL} (mF)	ECSA (cm^2)
$Fe_{0.1}$-NiO	6.5	163	18	450
$Co_{0.1}$-NiO	10	250	25	625
$Mn_{0.1}$-NiO	12	300	28	675
$Zn_{0.1}$-NiO	6	150	10	250

3.1.6 LSV comparison before and after OER.

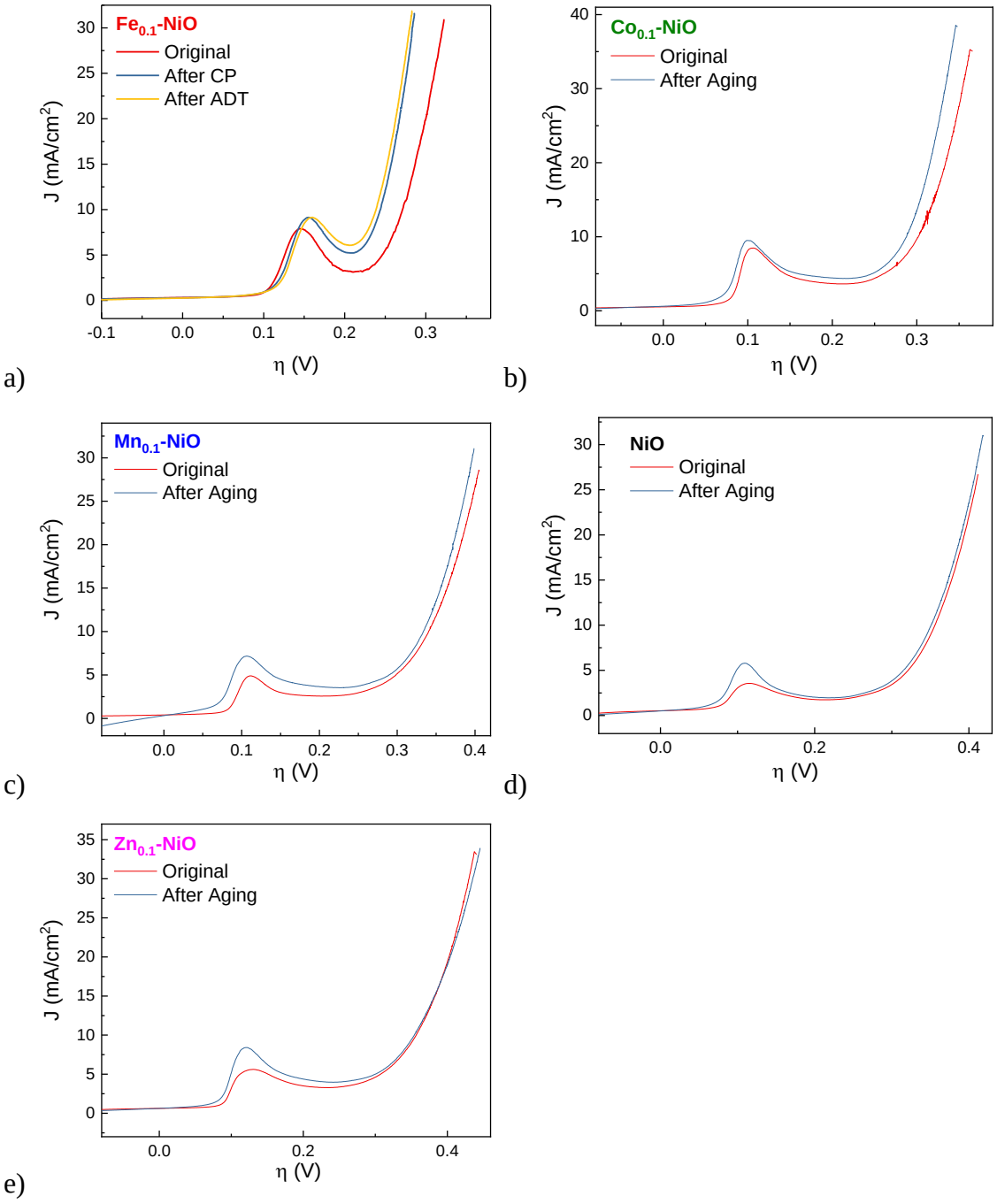

Figure S27. Electrochemical stability for $Fe_{0.1}$-NiO (a), $Co_{0.1}$-NiO (b), $Mn_{0.1}$-NiO (c), NiO(d) and $Zn_{0.1}$-NiO (d) before (red line) and after (blue line) 24 hours CP experiments and consecutive ADT tests. The samples were grown onto NF and tested at pH 13 (KOH 0.1 M).

Table S6. Summary of leaching tests carried out on the supernatant electrolyte.

Material	[Fe] (µM)	[Co] (µM)	[Mn] (µM)	[Ni] (µM)	[Zn] (µM)
Fe_{01}-NiO	< 0.1			< 0.1	
$Co_{0.1}$-NiO		< 0.1		< 0.1	
$Mn_{0.1}$-NiO			< 0.1	2.7	
NiO				< 0.1	
$Zn_{0.1}$-NiO				< 0.1	7

According to gravimetric determination before and after the electrode combustion, a catalyst loading of 1 mg/cm^2 was found. Under the assumption that the increment of weight is only due to the catalyst coating, in the case of 100% leaching, the final [Ni] in solution should be ca. 1.5 mM, whereas for the other metal cations it should correspond to 150 mM (total electrolyte volume = 9 mL). This indicates 0.2% Ni leaching in the case of $Mn_{0.1}$-NiO and Zn leaching of 4.6% in the case of $Zn_{0.1}$-NiO.

3.1.7 Fe_x-NiO.

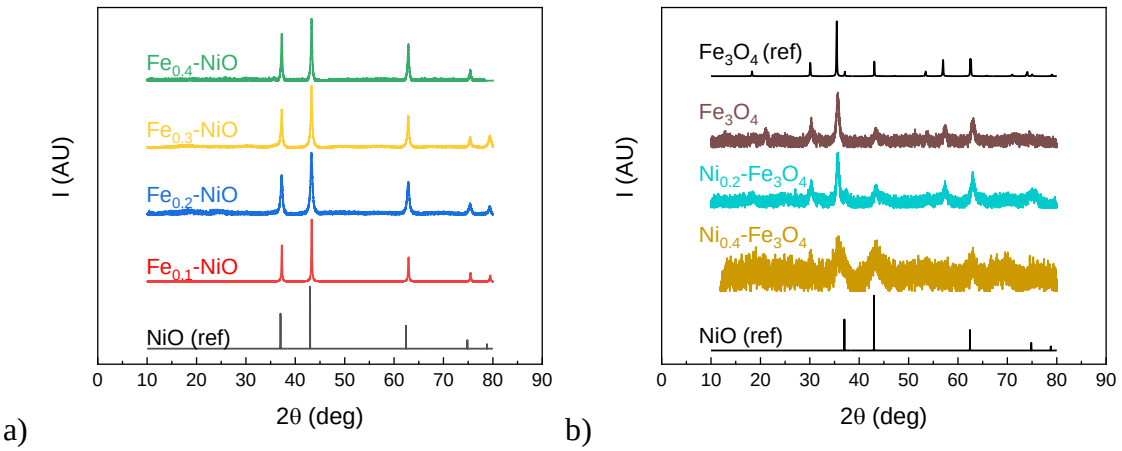

a) b)

Figure S28. (a) PXRD pattern of Fe-doped NiO systems with increasing Fe concentration. $Fe_{0.1}$-NiO (red), $Fe_{0.2}$-NiO (blue), $Fe_{0.3}$-NiO (yellow), $Fe_{0.4}$-NiO (green). Reference NiO (black) is reported on the bottom. (b) PXRD pattern of Ni-doped Fe_3O_4 with decreasing Ni concentration. $Ni_{0.4}$-Fe_3O_4 (gold), $Ni_{0.2}$-Fe_3O_4 (cyan), Fe_3O_4 (brown). NiO and Fe_3O_4 references are reported on top and bottom, respectively.

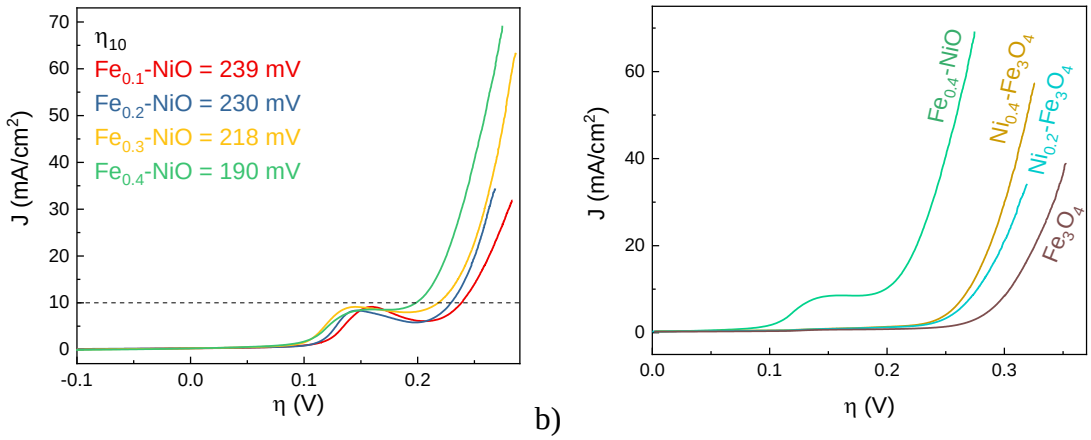

a) b)

Figure S29. (a) LSV polarization curves for Fe-doped NiO (Fe content = 10% (red); 20% (blue); 30% (yellow); 40% (green)). (b) LSV polarization curves for Ni-doped Fe_3O_4 (Ni content = 40% (gold), 20% (cyan) and 0% (brown)) and best-in-class $Fe_{0.4}$-NiO.

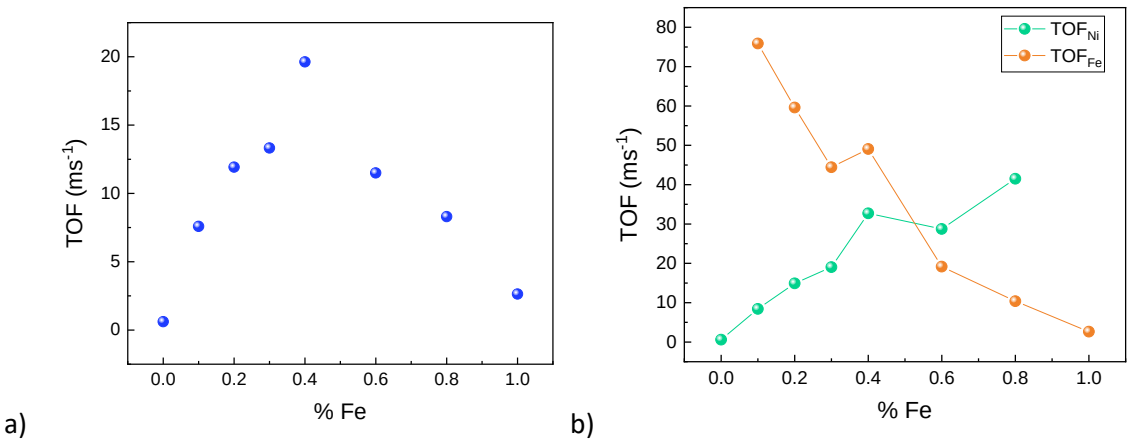

Figure S30. (a) TOF as a function of the Fe content and (b) disentanglement of the TOF from TOF_{Ni} and TOF_{Fe}. The TOF is calculated at $\eta = 275$ mV for all the systems, based on the calculated loadings of the samples (about 0.67 mg cm^{-2}).

3.1.8 Benchmarking.

Table S7. Benchmarking with best OER catalyst in the literature.

Material	***Support***	η_{10}	***Electrolyte***	***Ref***
$Fe_{0.4}$-NiO	NF	190	0.1 M KOH	*This Work*
$Fe_{0.3}$-NiO	NF	220	0.1 M KOH	*This Work*
$Fe_{0.2}$-NiO	NF	226	0.1 M KOH	*This Work*
$Fe_{0.1}$-NiO	NF	239	0.1 M KOH	*This Work*
$Ni_{0.4}$-Fe_3O_4	NF	269	0.1 M KOH	*This Work*
$Ni_{0.2}$-Fe_3O_4	NF	277	0.1 M KOH	*This Work*
Fe_3O_4	NF	304	0.1 M KOH	*This Work*
$Co_{0.1}$-NiO	NF	285	0.1 M KOH	*This Work*
$Mn_{0.1}$-NiO	NF	321	0.1 M KOH	*This Work*
NiO	NF	351	0.1 M KOH	*This Work*
$Zn_{0.1}$-NiO	NF	362	0.1 M KOH	*This Work*
$Fe(PO_3)_2$	NF	218	0.1 M KOH	*8*
Ni-Co Hydroxide	ITO	460	0.1 M KOH	*9*
NiFe LDH/CNTs	GC	308	0.1 M KOH	*10*
$CaCu_3Fe_4O_{12}$	GC	382	0.1 M KOH	*11*
$CoSe_2$	GC	320	0.1 M KOH	*12*
$CoSe_2$/N-Graphene	GC	366	0.1 M KOH	*13*
Co_3O_4/C	Cu Foam	290	0.1 M KOH	*14*
NiFe Hydroxides	NF	240	0.1 M KOH	*15*
FeP/Ni_2P	NF	154	1 M KOH	*16*
NiFeCP	NF	188	1 M KOH	*17*
NiCo-UMOFNs	CF	189	1 M KOH	*18*
NiFe-UMNs	GC	260	1 M KOH	*19*
NiFe (MIL-53)	NF	233	1 M KOH	*20*

NiFe-MOF	NF	240	1 M KOH	*21*
NiFe LDH/r-GO	NF	195	1 M KOH	*22*
Fe0.5Ni0.5	N-GR	210	1 M KOH	*23*
$Ni_{60}Fe_{30}Mn_{10}$		200	0.5 M KOH	*24*
$(Ni_{0.5}Fe_{0.5})_2P$	NF	η_{50} 251	1 M KOH	*25*
$Ni_{0.83}Fe_{0.17}(OH)_2$	GC	245	1 M KOH	*16*
NiFeMo	NF	238	1 M KOH	*26*
$Ni_xFe_{1-x}Se_2$-DO	NF	195	1 M KOH	*27*
NiFe LDH-NS	DG	210	1 M KOH	*28*

3.2 Characterization after OER.

3.2.1 PXRD after OER.

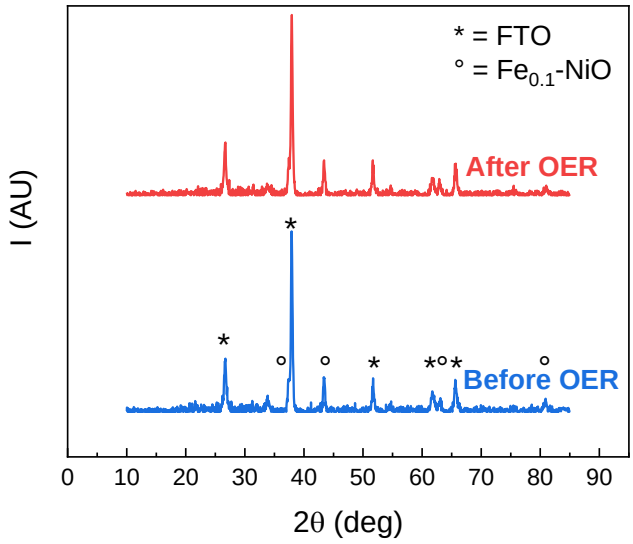

Figure S31. PXRD pattern of $Fe_{0.1}$-NiO before (blue) and after (red) OER.

3.2.2 STEM after OER.

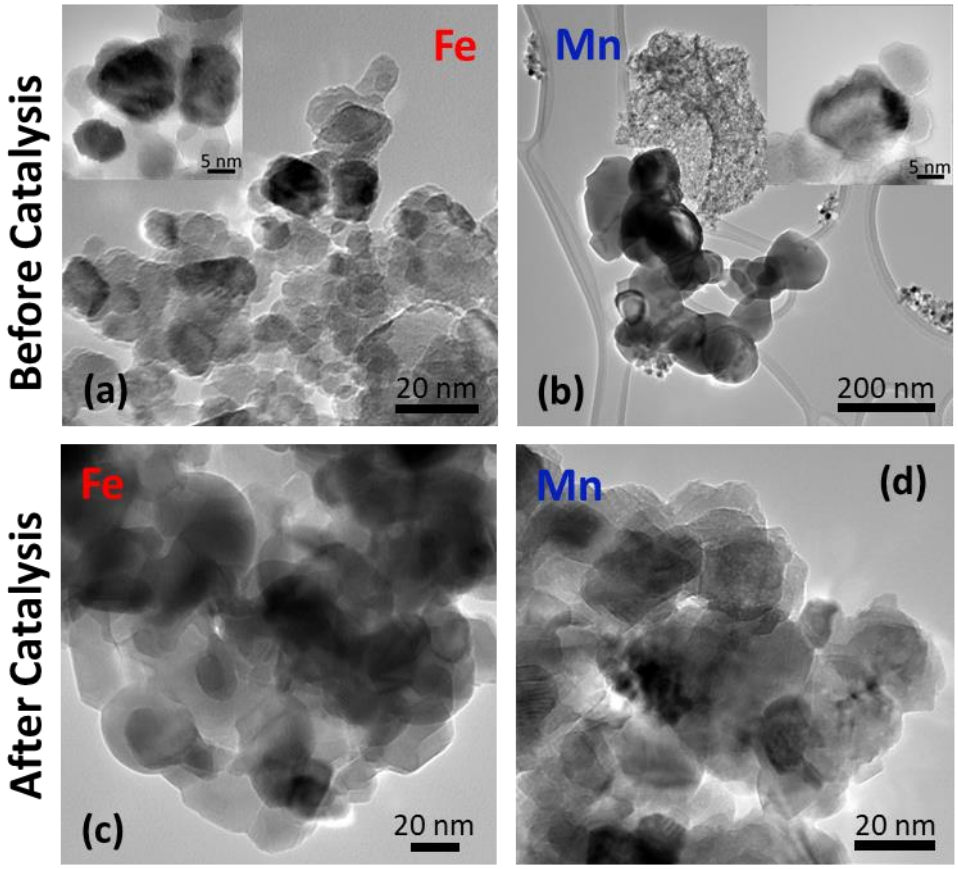

Figure S32. STEM images of the Fe- (a, c) and Mn- (b, d) doped NiO before (upper row) and after (lower row) driving the OER.

3.2.3 SEM images after OER.

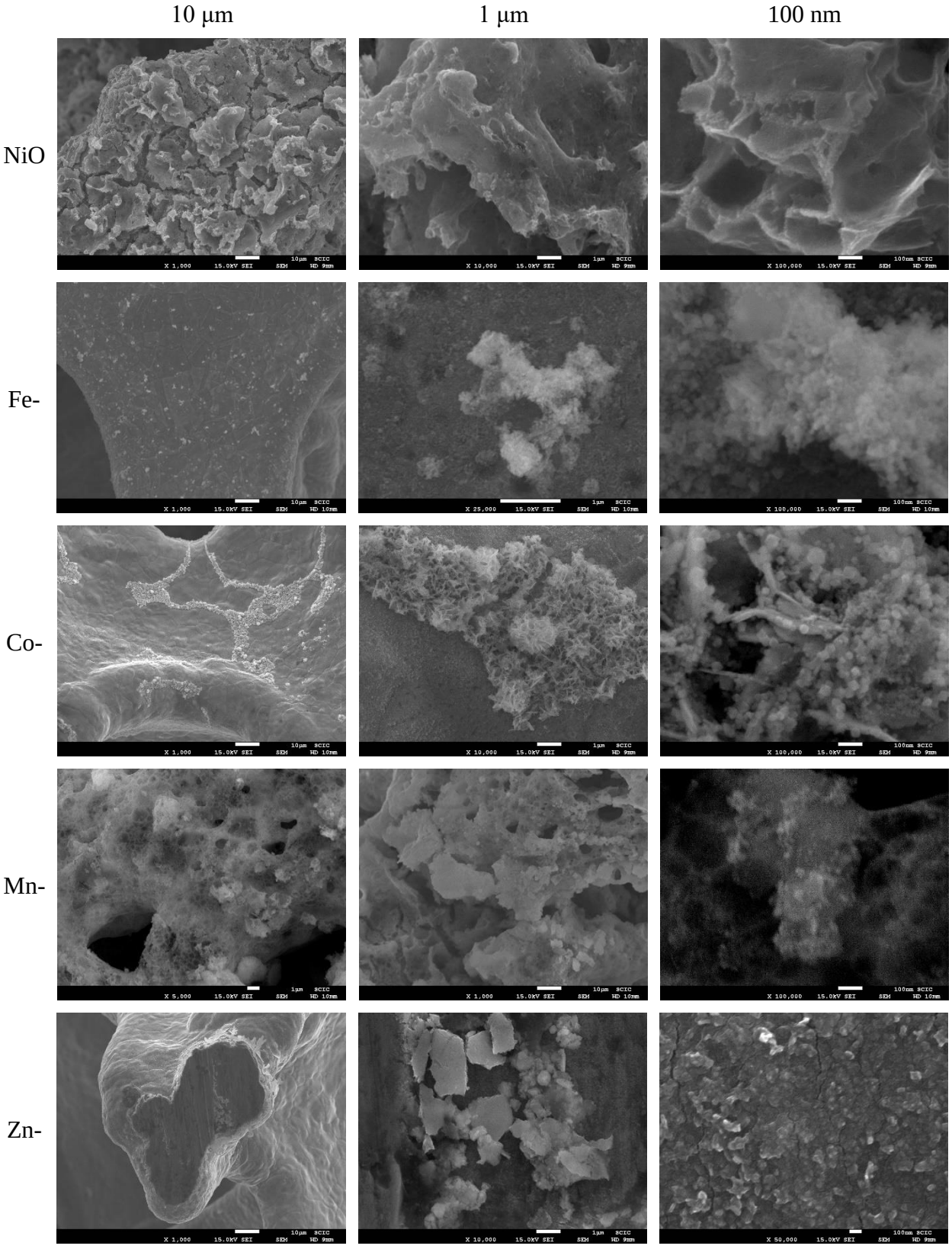

Figure S33. SEM images of (from first to the last row) NiO/NF, $Fe_{0.1}$-NiO/NF, $Co_{0.1}$-NiO/NF, $Mn_{0.1}$-NiO/NF and $Zn_{0.1}$-NiO/NF, respectively, after OER at a different level of magnification.

3.2.4 Raman after OER.

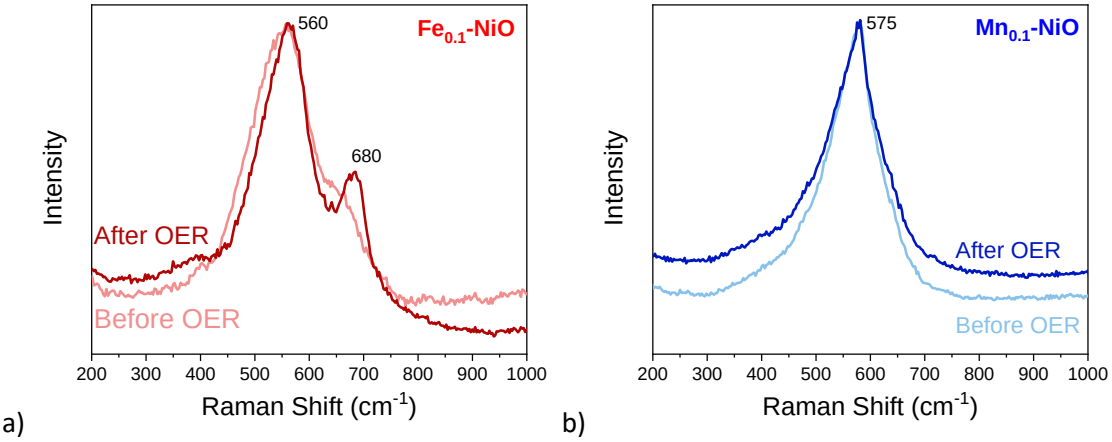

Figure S34. Raman spectra of the Fe and Mn doped NiOx electrocatalysts acquired (a) before and (b) after OER (chronoamperometric test of 30 min at 2 V vs RHE).

3.2.5 XPS after OER.

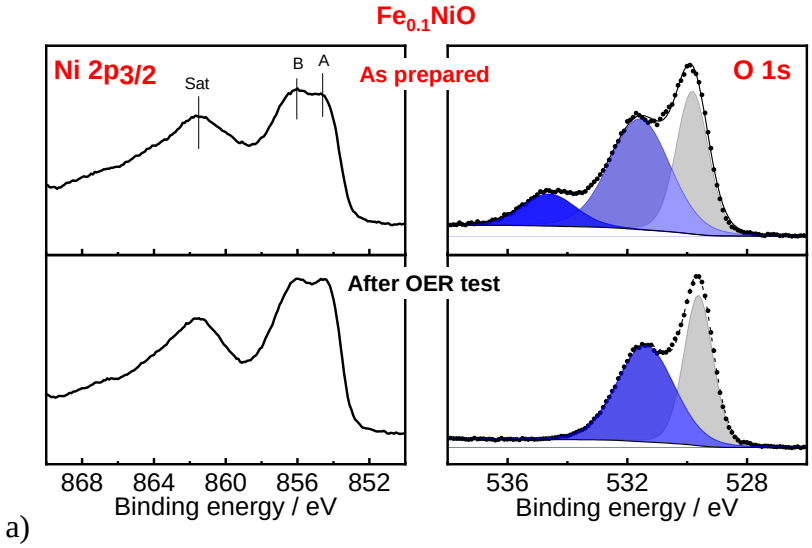

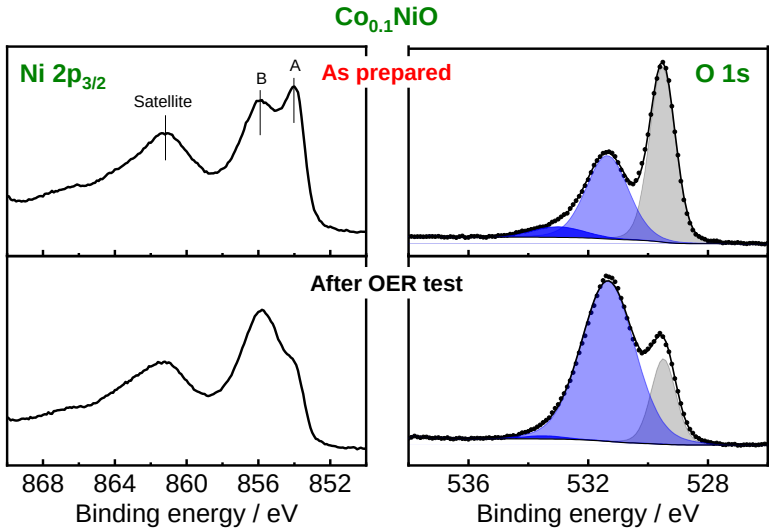
Co0.1NiO
Ni 2p3/2
Satellite
B
A
As prepared
O 1s
After OER test
868 864 860 856 852
Binding energy / eV
536 532 528
Binding energy / eV

b)

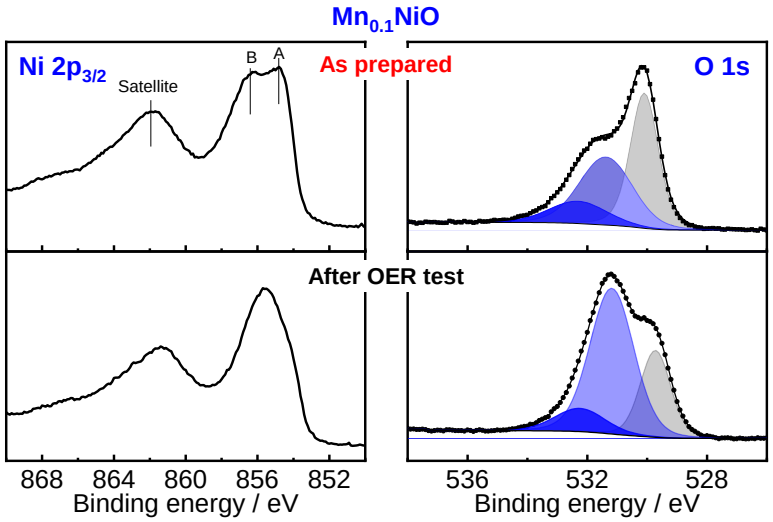
Mn0.1NiO
Ni 2p3/2
Satellite
B
A
As prepared
O 1s
After OER test
868 864 860 856 852
Binding energy / eV
536 532 528
Binding energy / eV

c)

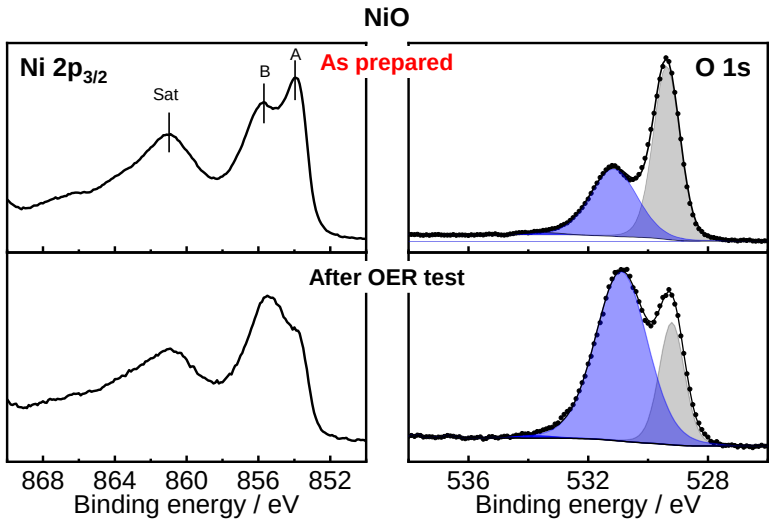
NiO
Ni 2p3/2
Sat
B
A
As prepared
O 1s
After OER test
868 864 860 856 852
Binding energy / eV
536 532 528
Binding energy / eV

d)

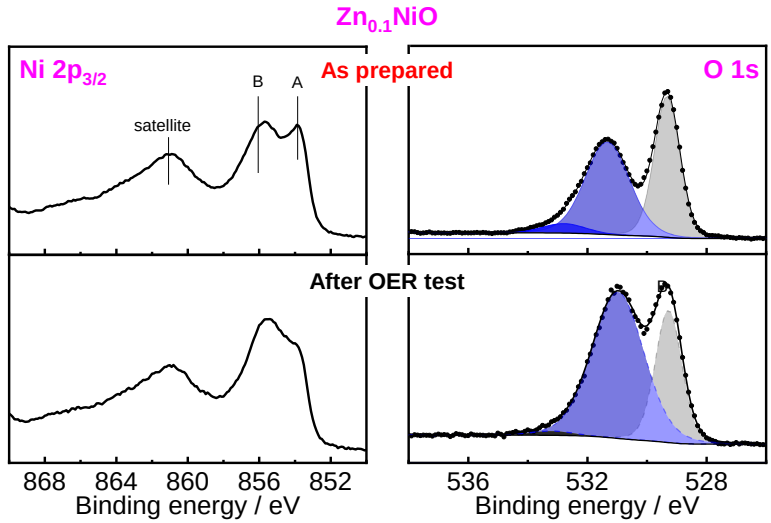

e)

Figure S35. XPS spectrum of Ni $2p_{3/2}$ (left) and O 1s (right) for $Fe_{0.1}$-NiO (a), $Co_{0.1}$-NiO (b), $Mn_{0.1}$-NiO (c), NiO (d), $Zn_{0.1}$-NiO (e) before and after OER.

3.3 (M)-NiO/FTO

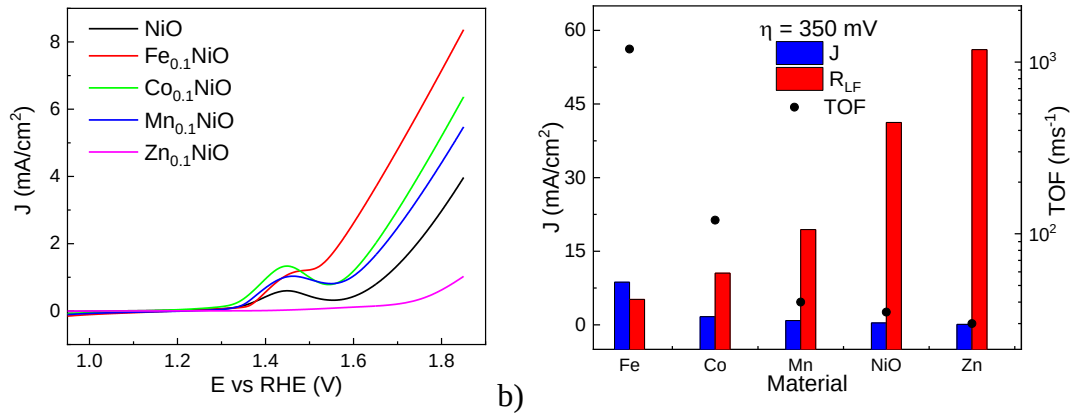

Figure S36. Performance comparison between NiO and M-NiO on FTO in KOH pH 13. Panel a) shows polarization curves (collected at 5 mVs^{-1}), whereas in panel b) the main kinetic parameters are summarized (ie. current density, charge-transfer resistance and TOF_{redox}) obtained for η = 350 mV.

3.3.1 Determination of Tafel slopes on FTO-plated samples.

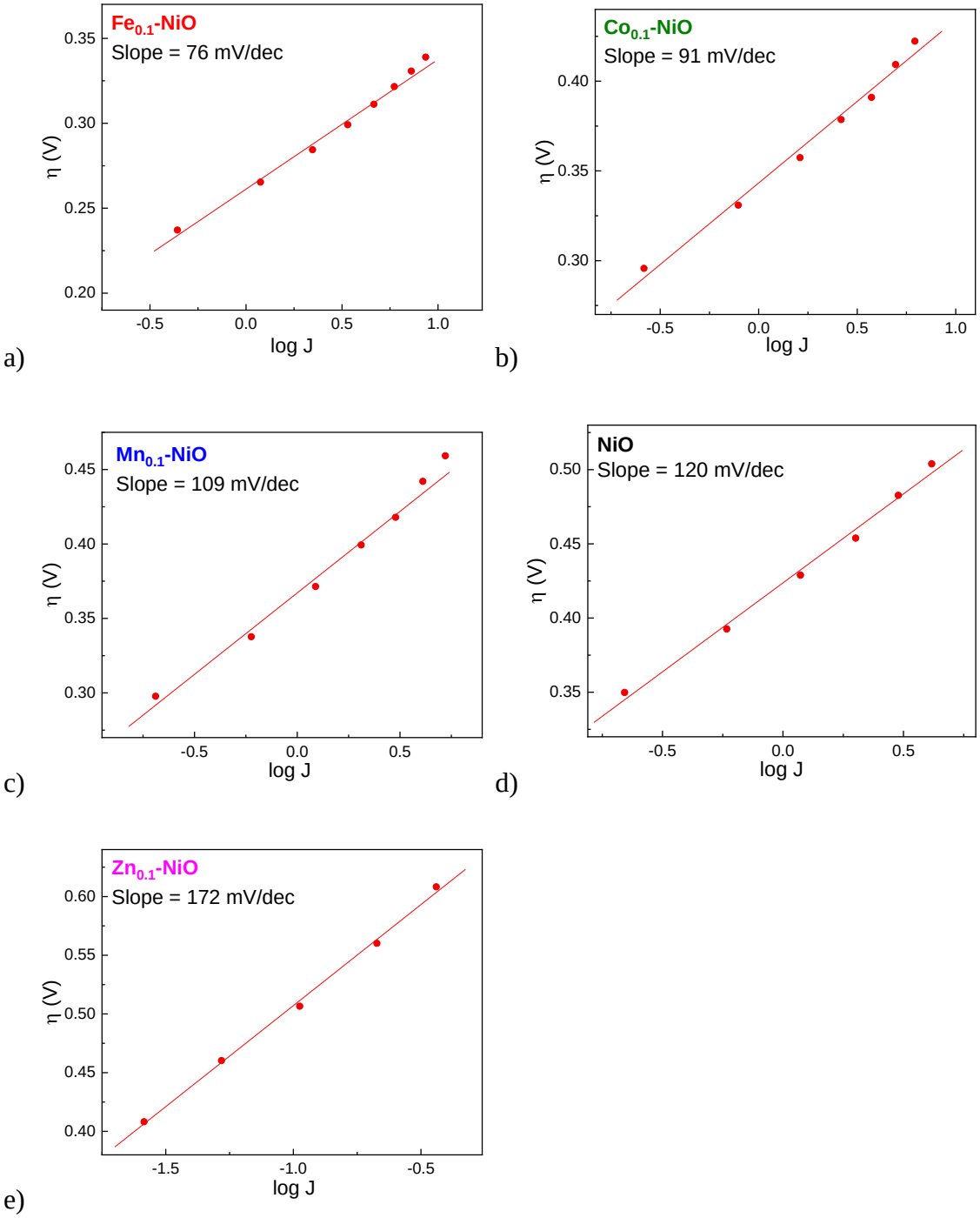

Figure S37. Tafel plots for $Fe_{0.1}$-NiO/FTO (a), $Co_{0.1}$-NiO/FTO (b), $Mn_{0.1}$-NiO/FTO (c), NiO/FTO (d) and $Zn_{0.1}$-NiO/FTO (e) samples. The Tafel slope indicated inside the individual graphs well matches with the one reported for the catalysts grown in NF.

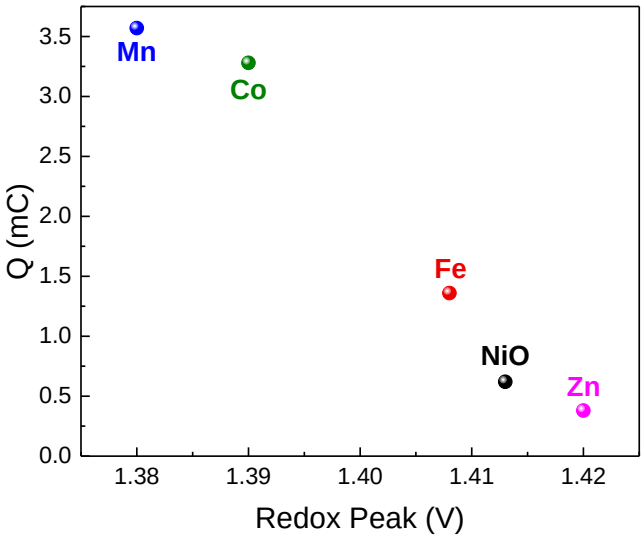

Figure S38. Correlation between the position of the anodic redox peak for Ni^{2+}/Ni^{3+} couple and the integrated charge.

3.3.2 Comparison LSV before and after OER on FTO-plated samples.

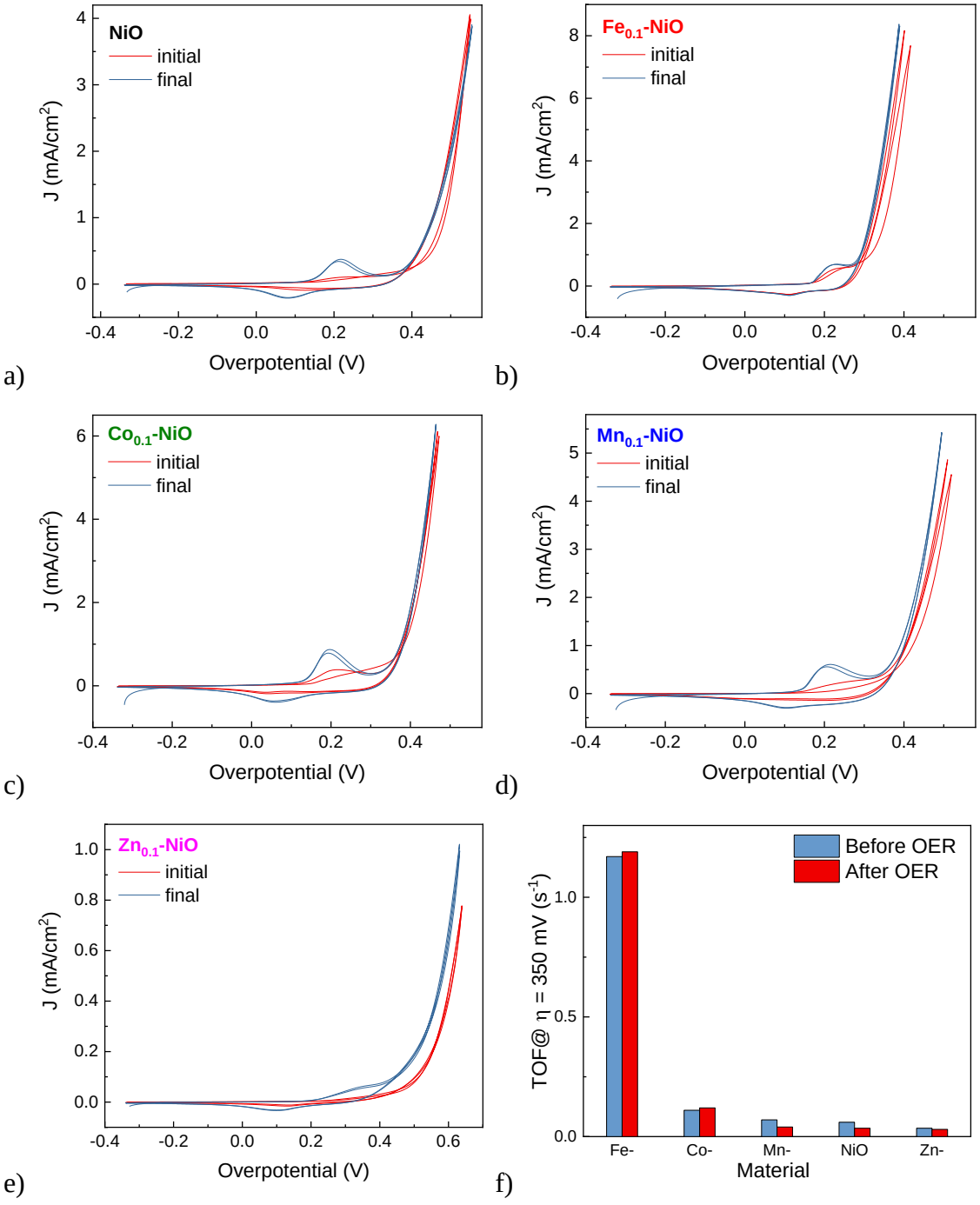

Figure S39. (a-e) Cyclic Voltammetry of NiO and M-NiO showing the changes of the electrochemical features during the measures. Panel f) offers a comparison in the TOF_{redox} values calculated at $\eta = 350$ mV before and after electrochemical aging.

3.3.3 Impedance Spectroscopy (EIS) for FTO-plated samples.

In general, Nyquist plots show two semicircles, so the impedance response is described by the Armstrong-Henderson equivalent circuit to account for low-frequency intermediate adsorption processes (Figure S40a).[29-32] Conversely, in the case of $Zn_{0.1}$-NiO a simple Randles' circuit was used since only one semicircle appears (Figure S40b).

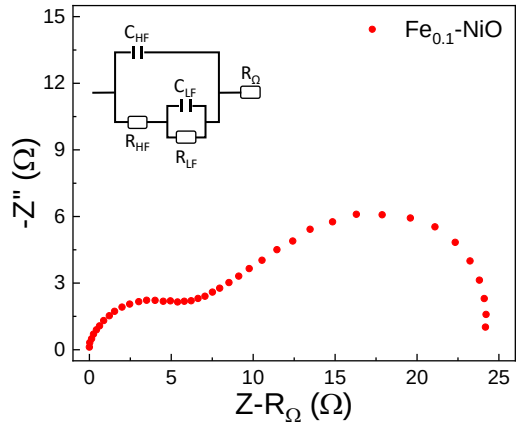

a)

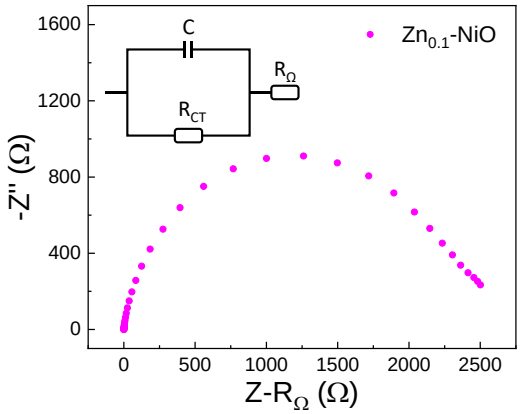

b)

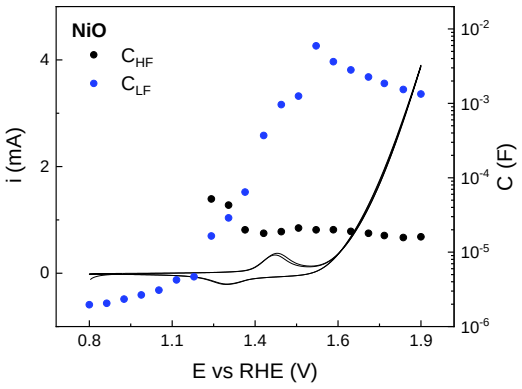

c)

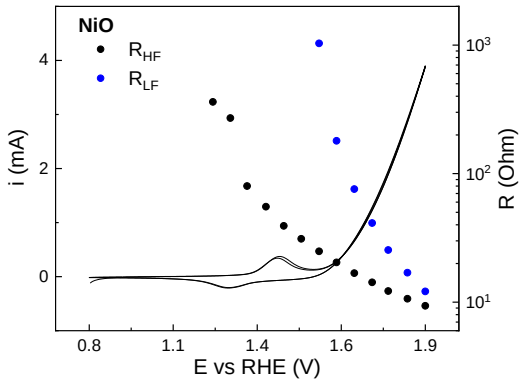

d)

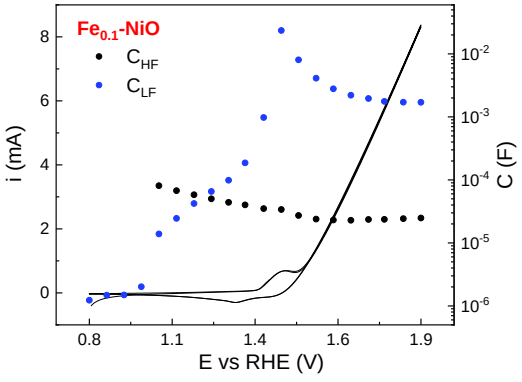

e)

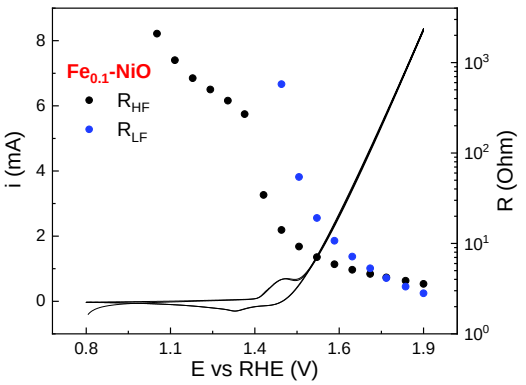

f)

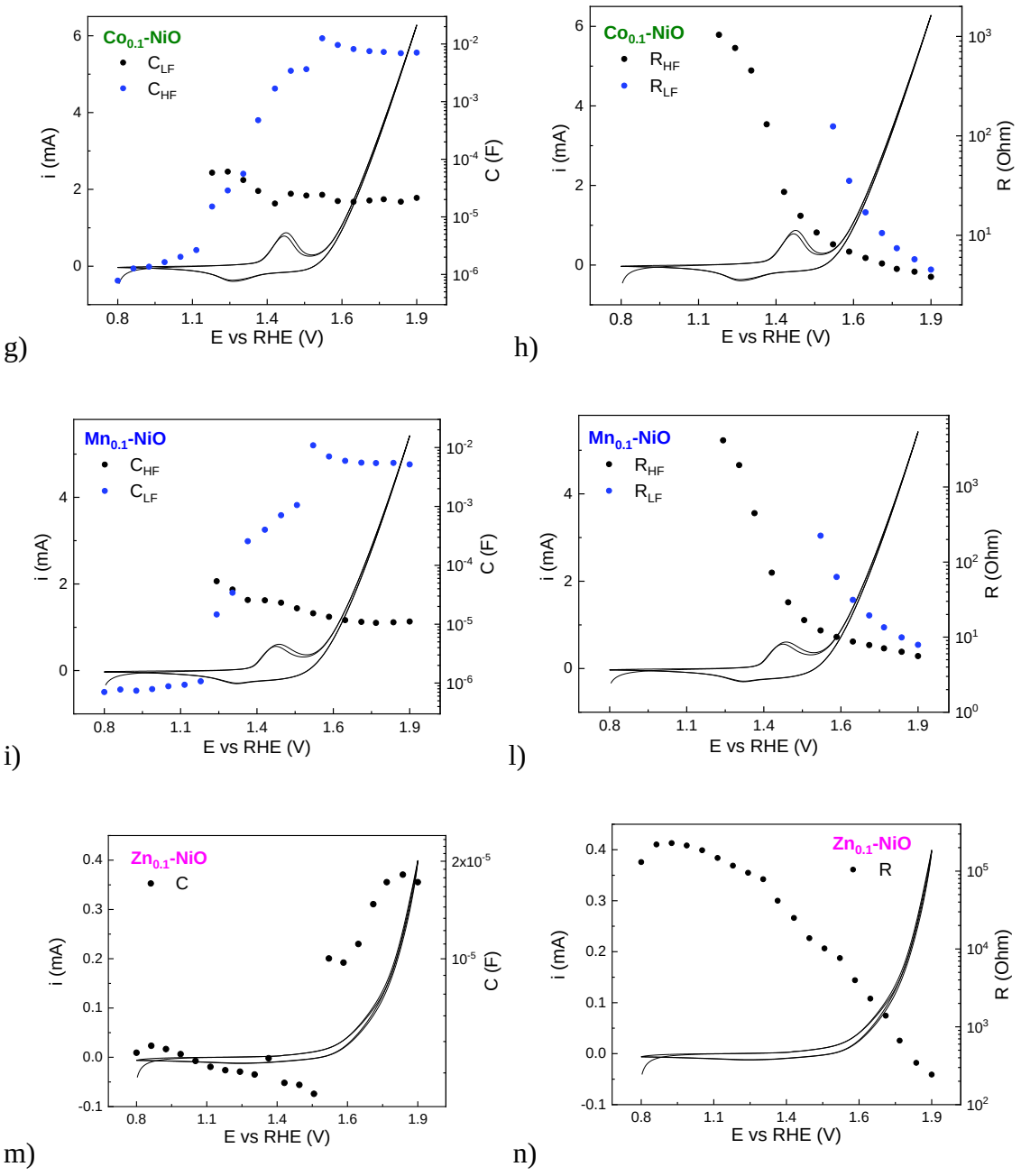

Figure S40. a) Randles circuit used for fitting EIS data for $Zn_{0.1}$-NiO and b) Voight model used for the other cases. Panels from c) to n) show the trend of C with the potential (left) and R vs E (right).

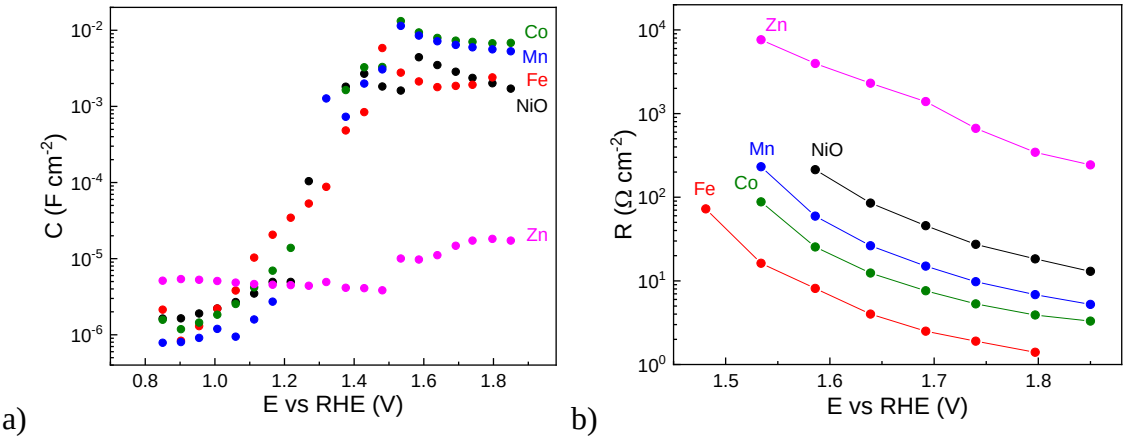

Figure S41. Comparison in the evolution of the capacitance (a) and the resistance (b) as a function of applied potential for M-NiO@FTO.

Table S8. Resume of fitted parameters derived by EIS.

E vs RHE	NiO				$Fe_{0.1}$-NiO				$Co_{0.1}$-NiO			
	R_{HF}	C_{HF}	R_{LF}	C_{LF}	R_{HF}	C_{HF}	R_{LF}	C_{LF}	R_{HF}	C_{HF}	R_{LF}	C_{LF}
V	Ω	μF	Ω	mF	Ω	μF	Ω	mF	Ω	μF	Ω	mF
0.82	-	-	-	0.0				0.0				0
0.87	-	-	-	0.0				0.0				0
0.93	-	-	-	0.0				0.0				0
0.98	-	-	-	0.0				0.0				0
1.03	-	-	-	0.0	2089	81		0.0				0
1.08	-	-	-	0.0	1062	67		0.0				0
1.14	-	-	-	0.0	672	58		0.0	1037	58		0
1.19	361	52	-	0.0	503	50		0.1	765	61		0
1.24	271	43	-	0.0	379	44		0.1	454	44		0
1.29	80	20	-	0.1	269	40		0.2	131	28		0
1.35	55	18	-	0.4	34	35		1.0	27	17		2
1.40	39	19	-	1.0	14	34	577	23.5	16	25		3
1.45	31	21	-	1.3	9	27	54	8.1	11	23		4
1.50	25	20	1032	5.9	7	24	19	4.1	8	24	125	13

1.56	20	20	180	3.6	6	23	11	2.8	7	19	35	10
1.61	17	19	76	2.8	5	23	7	2.2	6	18	17	8
1.66	14	18	41	2.3	5	24	5	2.0	5	19	11	8
1.71	12	17	25	1.9	4	24	4	1.8	5	20	7	7
1.77	11	16	17	1.5	4	24	3	1.7	4	18	6	7
1.82	9	16	12	1.3	4	25	3	1.7	4	21	5	7

E vs RHE	$Mn_{0.1}$-NiO				$Zn_{0.1}$-NiO	
V	R_{HF}	C_{HF}	R_{LF}	C_{LF}	R	C_{DL}
	Ω	μF	Ω	mF	Ω	μF
0.82	4180			0	130560	5
0.87	1955			0	219950	5
0.93	448			0	229050	5
0.98	72			0	213200	5
1.03	29			0	185420	5
1.08	17			0	147410	5
1.14	12			0	117410	5
1.19	10	54		0	95193	4
1.24	9	39		0	78654	4
1.29	8	26		0	41624	5
1.35	7	25		0	25034	4
1.40	6	23		1	13766	4
1.45	6	19		1	10152	4
1.50	4180	15	224	11	7629	10
1.56	1955	13	63	7	3966	10
1.61	448	12	31	6	2302	11
1.66	72	11	19	6	1389	15
1.71	29	11	13	5	665	17
1.77	17	11	10	5	344	18
1.82	12	11	8	5	243	17

Three different regions can be identified. The non-faradic one (0.8 V < V < 1.3 V), the redox region, including Ni^{2+} features (1.3 V < V < V_{onset}, pre-catalytic region) and lastly the OER region (V_{onset} < V, catalytic region). Whereas for $Zn_{0.1}$-NiO, C decreases until OER begins, in the other cases the low-frequency capacitance increases with the potential, describing a shoulder before OER regions and then a peak when the potential is close to the onset of oxygen evolution. In the non-faradic region, the highest capacitance belongs to $Zn_{0.1}$-NiO, followed by NiO, Fe, Co and Mn. Interestingly, this order is basically inverted in the OER region, where the capacitance increases with the order Zn < Fe ≈ NiO < Mn < Co. As expected, all the double-layer capacitances measured in FTO are much lower than those reported for NF, since the latter is a 3D material, whereas FTO is a plain surface, but in the case of $Zn_{0.1}$-NiO, there is an inversion in the trend and its incredibly low capacitance in FTO is the lowest of the family. This suggests that the effect of growing due material onto the current collector is beneficial for the catalysis.

3.3.4 Mott-Schottky analysis for FTO-plated samples

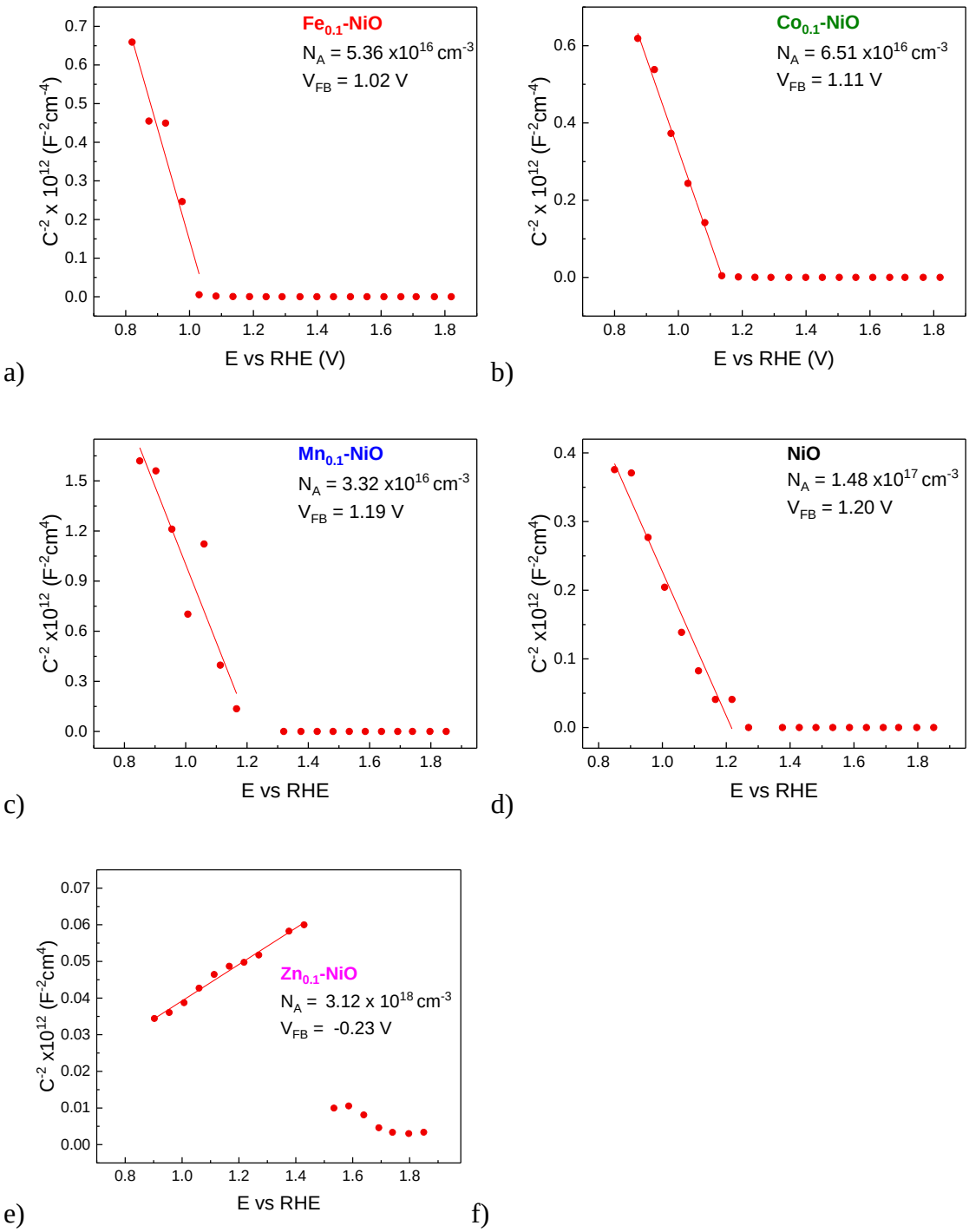

Figure S42. Mott-Schottky analysis for $Fe_{0.1}$-NiO (a), $Co_{0.1}$-NiO (b), $Mn_{0.1}$-NiO (c), NiO (d) and $Zn_{0.1}$-NiO (e). The values of the different slopes and flat band potentials are summarized in panel (f).

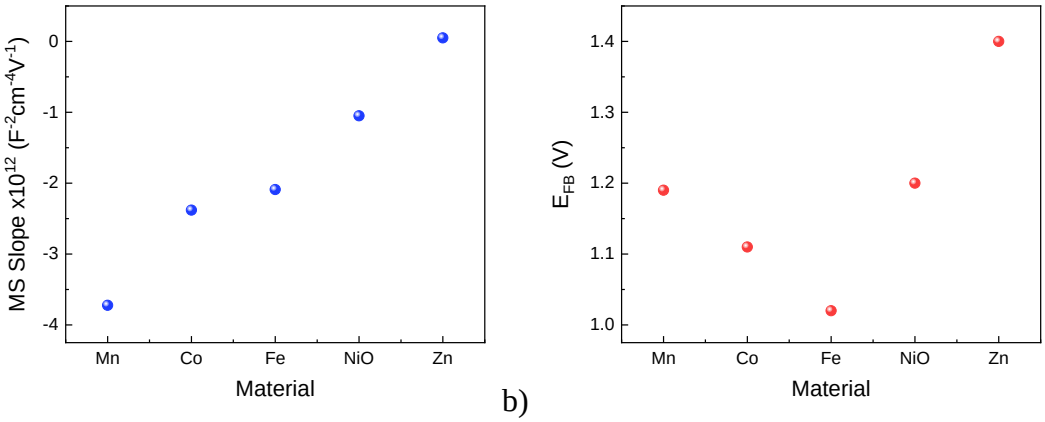

Figure S43. The values of the different slopes (a) and flat band potentials (b) for M-NiO materials.

Table S9. Summary of the Mott-Schottky Parameters

Material	N_A x 10^{16} cm^{-3}	E_{FB} (V vs RHE)
$Fe_{0.1}$-NiO	5.36	1.02
$Co_{0.1}$-NiO	6.51	1.11
$Mn_{0.1}$-NiO	3.32	1.19
NiO	14.8	1.20
$Zn_{0.1}$-NiO	312	0.23

3.3.5 Spectroelectrochemistry (SEC) for FTO-plated samples

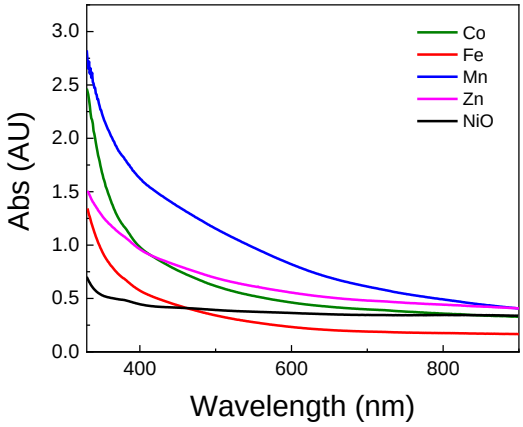

Figure S44: UV/Vis absorption of each catalyst

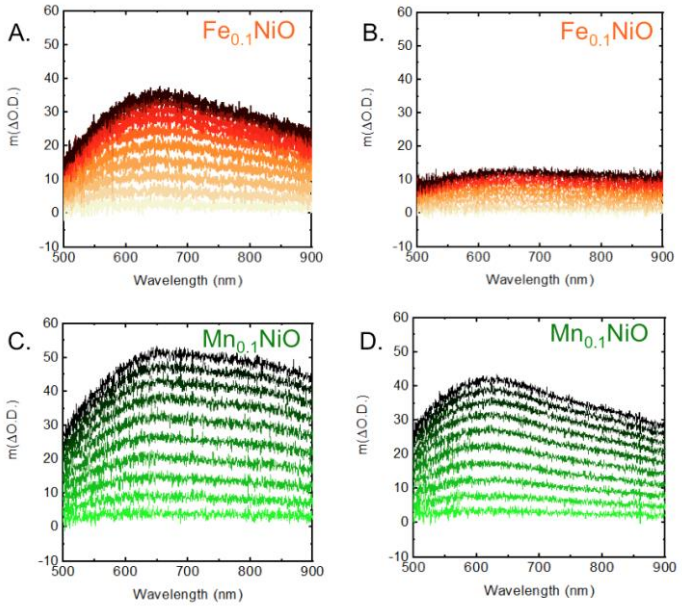

Figure S45: Spectroelectrochemistry of $Fe_{0.1}$-NiO (a,b, two different points on the same sample) and $Mn_{0.1}$-NiO (c,d, two different points on the same sample) on FTO prepared by solution combustion synthesis. The inhomogeneity of the samples results in different absorption changes on the same sample.

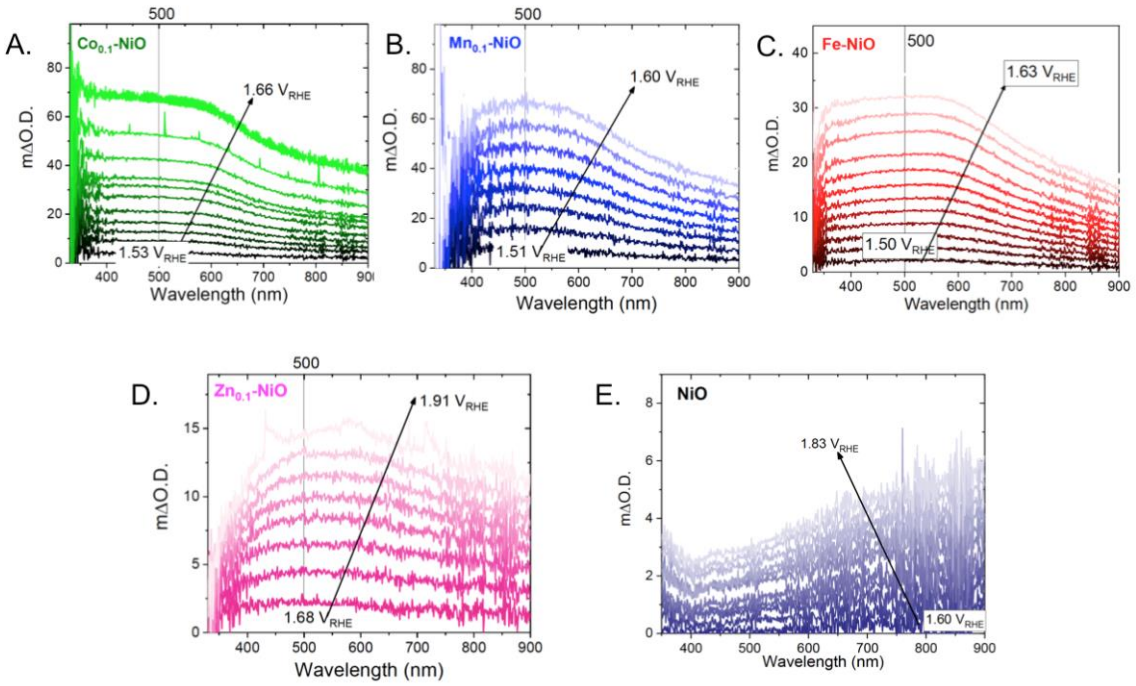

Figure S46. Spectroelectrochemistry of (a) $Co_{0.1}$-NiO, (b) $Mn_{0.1}$-NiO, (c) $Fe_{0.1}$-NiO and (d) $Zn_{0.1}$-NiO and (e) NiO over catalytic potentials. (0.1 M pure KOH).

By subtracting the spectra at catalytic potentials (~1.6 V_{RHE}) from the spectrum at the onset of catalysis, the spectra of the species accumulated during steady-state water oxidation were obtained.

References

1. Ravel, B.; Newville, M., ATHENA, ARTEMIS, HEPHAESTUS: data analysis for X-ray absorption spectroscopy using IFEFFIT. *J. Synchrotron Radiat.* **2005,** *12*, 537-541.
2. Newville, M., EXAFS analysis using FEFF and FEFFIT. *J. Synchrotron Radiat.* **2001,** *8*, 96-100.
3. Rehr, J. J.; Albers, R. C., Theoretical approaches to x-ray absorption fine structure. *Reviews of Modern Physics* **2000,** *72* (3), 621-654.
4. Newville, M., Larch: An analysis package for XAFS and related spectroscopies. *Journal of Physics: Conference Series* **2013,** *430*.

5. Martin-Diaconescu, V.; Bellucci, M.; Musiani, F.; Ciurli, S.; Maroney, M. J., Unraveling the Helicobacter pylori UreG zinc binding site using X-ray absorption spectroscopy (XAS) and structural modeling. *J. Biol. Inorg. Chem.* **2012,** *17* (3), 353-361.
6. Zambelli, B.; Berardi, A.; Martin-Diaconescu, V.; Mazzei, L.; Musiani, F.; Maroney, M. J.; Ciurli, S., Nickel binding properties of Helicobacter pylori UreF, an accessory protein in the nickel-based activation of urease. *J. Biol. Inorg. Chem.* **2014,** *19* (3), 319-334.
7. Rao, K. V.; Smakula, A., Dielectric Properties of Cobalt Oxide, Nickel Oxide, and Their Mixed Crystals. *J. Appl. Phys.* **1965,** *36* (6), 2031-2038.
8. Zhou, H.; Yu, F.; Sun, J.; He, R.; Chen, S.; Chu, C.-W.; Ren, Z., Highly active catalyst derived from a 3D foam of $Fe(PO_3)_2/Ni_2P$ for extremely efficient water oxidation. *Proc. Natl. Acad. Sci. U. S. A.* **2017,** *114* (22), 5607.
9. Zhao, Z.; Wu, H.; He, H.; Xu, X.; Jin, Y., A High-Performance Binary Ni–Co Hydroxide-based Water Oxidation Electrode with Three-Dimensional Coaxial Nanotube Array Structure. *Adv. Funct. Mater.* **2014,** *24* (29), 4698-4705.
10. Gong, M.; Li, Y.; Wang, H.; Liang, Y.; Wu, J. Z.; Zhou, J.; Wang, J.; Regier, T.; Wei, F.; Dai, H., An Advanced Ni–Fe Layered Double Hydroxide Electrocatalyst for Water Oxidation. *J. Am. Chem. Soc.* **2013,** *135* (23), 8452-8455.
11. Yagi, S.; Yamada, I.; Tsukasaki, H.; Seno, A.; Murakami, M.; Fujii, H.; Chen, H.; Umezawa, N.; Abe, H.; Nishiyama, N.; Mori, S., Covalency-reinforced oxygen evolution reaction catalyst. *Nat. Comm.* **2015,** *6* (1), 8249.
12. Liu, Y.; Cheng, H.; Lyu, M.; Fan, S.; Liu, Q.; Zhang, W.; Zhi, Y.; Wang, C.; Xiao, C.; Wei, S.; Ye, B.; Xie, Y., Low Overpotential in Vacancy-Rich Ultrathin CoSe2 Nanosheets for Water Oxidation. *J. Am. Chem. Soc.* **2014,** *136* (44), 15670-15675.
13. Gao, M.-R.; Cao, X.; Gao, Q.; Xu, Y.-F.; Zheng, Y.-R.; Jiang, J.; Yu, S.-H., Nitrogen-Doped Graphene Supported CoSe2 Nanobelt Composite Catalyst for Efficient Water Oxidation. *ACS Nano* **2014,** *8* (4), 3970-3978.
14. Ma, T. Y.; Dai, S.; Jaroniec, M.; Qiao, S. Z., Metal–Organic Framework Derived Hybrid Co3O4-Carbon Porous Nanowire Arrays as Reversible Oxygen Evolution Electrodes. *J. Am. Chem. Soc.* **2014,** *136* (39), 13925-13931.
15. Lu, X.; Zhao, C., Electrodeposition of hierarchically structured three-dimensional nickel–iron electrodes for efficient oxygen evolution at high current densities. *Nat. Comm.* **2015,** *6* (1), 6616.
16. Yu, F.; Zhou, H.; Huang, Y.; Sun, J.; Qin, F.; Bao, J.; Goddard, W. A.; Chen, S.; Ren, Z., High-performance bifunctional porous non-noble metal phosphide catalyst for overall water splitting. *Nat. Comm.* **2018,** *9* (1), 2551.
17. Li, W.; Li, F.; Yang, H.; Wu, X.; Zhang, P.; Shan, Y.; Sun, L., A bio-inspired coordination polymer as outstanding water oxidation catalyst via second coordination sphere engineering. *Nat. Comm.* **2019,** *10* (1), 5074.
18. Zhao, S.; Wang, Y.; Dong, J.; He, C.-T.; Yin, H.; An, P.; Zhao, K.; Zhang, X.; Gao, C.; Zhang, L.; Lv, J.; Wang, J.; Zhang, J.; Khattak, A. M.; Khan, N. A.; Wei, Z.; Zhang, J.; Liu, S.; Zhao, H.; Tang, Z., Ultrathin metal–organic framework nanosheets for electrocatalytic oxygen evolution. *Nat. Energy* **2016,** *1* (12), 16184.
19. Hai, G.; Jia, X.; Zhang, K.; Liu, X.; Wu, Z.; Wang, G., High-performance oxygen evolution catalyst using two-dimensional ultrathin metal-organic frameworks nanosheets. *Nano Energy* **2018,** *44*, 345-352.
20. Sun, F.; Wang, G.; Ding, Y.; Wang, C.; Yuan, B.; Lin, Y., NiFe-Based Metal–Organic Framework Nanosheets Directly Supported on Nickel Foam Acting as Robust

Electrodes for Electrochemical Oxygen Evolution Reaction. *Adv. Energy Mater.* **2018,** *8* (21), 1800584.
21. Duan, J.; Chen, S.; Zhao, C., Ultrathin metal-organic framework array for efficient electrocatalytic water splitting. *Nat. Comm.* **2017,** *8* (1), 15341.
22. Long, X.; Li, J.; Xiao, S.; Yan, K.; Wang, Z.; Chen, H.; Yang, S., A Strongly Coupled Graphene and FeNi Double Hydroxide Hybrid as an Excellent Electrocatalyst for the Oxygen Evolution Reaction. *Angew. Chem. Int. Ed.* **2014,** *53* (29), 7584-7588.
23. Liu, P.; Gao, D.; Xiao, W.; Ma, L.; Sun, K.; Xi, P.; Xue, D.; Wang, J., Self-Powered Water-Splitting Devices by Core–Shell NiFe@N-Graphite-Based Zn–Air Batteries. *Adv. Funct. Mater.* **2018,** *28* (14), 1706928.
24. Detsi, E.; Cook, J. B.; Lesel, B. K.; Turner, C. L.; Liang, Y.-L.; Robbennolt, S.; Tolbert, S. H., Mesoporous Ni60Fe30Mn10-alloy based metal/metal oxide composite thick films as highly active and robust oxygen evolution catalysts. *Energy Environ. Sci.* **2016,** *9* (2), 540-549.
25. Yu, J.; Cheng, G.; Luo, W., Hierarchical NiFeP microflowers directly grown on Ni foam for efficient electrocatalytic oxygen evolution. *J. Mater. Chem. A* **2017,** *5* (22), 11229-11235.
26. Qin, F.; Zhao, Z.; Alam, M. K.; Ni, Y.; Robles-Hernandez, F.; Yu, L.; Chen, S.; Ren, Z.; Wang, Z.; Bao, J., Trimetallic NiFeMo for Overall Electrochemical Water Splitting with a Low Cell Voltage. *ACS Energy Lett.* **2018,** *3* (3), 546-554.
27. Xu, X.; Song, F.; Hu, X., A nickel iron diselenide-derived efficient oxygen-evolution catalyst. *Nat. Comm.* **2016,** *7* (1), 12324.
28. Meng, Q.; Yang, J.; Ma, S.; Zhai, M.; Lu, J., A Porous Cobalt (II) Metal–Organic Framework with Highly Efficient Electrocatalytic Activity for the Oxygen Evolution Reaction. *Polymers* **2017,** *9* (12), 676.
29. Armstrong, R. D.; Henderson, M., Impedance plane display of a reaction with an adsorbed intermediate. *J. Electroanal. Chem. Interf. Electrochem.* **1972,** *39* (1), 81-90.
30. Chakthranont, P.; Kibsgaard, J.; Gallo, A.; Park, J.; Mitani, M.; Sokaras, D.; Kroll, T.; Sinclair, R.; Mogensen, M. B.; Jaramillo, T. F., Effects of Gold Substrates on the Intrinsic and Extrinsic Activity of High-Loading Nickel-Based Oxyhydroxide Oxygen Evolution Catalysts. *ACS Catal.* **2017,** *7* (8), 5399-5409.
31. Garcia, A. C.; Touzalin, T.; Nieuwland, C.; Perini, N.; Koper, M. T. M., Enhancement of Oxygen Evolution Activity of Nickel Oxyhydroxide by Electrolyte Alkali Cations. *Angew. Chem. Int. Ed.* **2019,** *58* (37), 12999-13003.
32. Lyons, M. E. G.; Brandon, M. P., The Oxygen Evolution Reaction on Passive Oxide Covered Transition Metal Electrodes in Aqueous Alkaline Solution. Part 1-Nickel. *Int. J. Electrochem. Sci.* **2008,** *3* (12), 1386-1424.